

Imperial College  
London

EPFL



IMPERIAL COLLEGE LONDON

ÉCOLE POLYTECHNIQUE FÉDÉRALE DE LAUSANNE

DEPARTMENT OF PHYSICS

---

# Transition Crossing by Means of Stable Islands

---

*Author:*

Sabrina Wang (CID:01854074)

*Supervisor:*

Massimo Giovannozzi,  
Tatiana Pieloni

Word Count: 10997

Thesis submitted for the degree of

*MSci Physics with a Year Abroad*

July 3, 2023



## Abstract

The phenomenon of transition energy crossing might generate adverse effects to the quality of charged-particle beams in circular accelerators that is hard to avoid, and has been known to introduce potentially adverse disturbance to the longitudinal dynamics of a beam of charged particles. A novel method to cross the transition energy using non-linear magnets is simulated in this project on a realistic lattice of the CERN Super Proton Synchrotron (SPS). Through scans of the non-linear magnet parameters, two approaches to the solution are proposed which might be suitable for bringing the beam through the transition process. However, tight constraints on the beam result in significant beam-size growth when using these configurations and risk of the process being ineffective. The first approach maximises the transition energy difference to minimise the effects near transition. It has an energy difference of 0.118 GeV but a large emittance growth (beam size) of 749%. The second approach minimises the emittance growth, it gives an energy difference of 0.052 GeV and 150% emittance growth. These results demonstrate the feasibility of the method, identifies the limitations and further work to minimise the emittance growth.

# Preface

The work is carried out at the CERN Beams Department, in the Accelerator and Beams Physics (ABP) Group, with the Non-linear Dynamics and Collimation (NDC) Section and the Laboratory of Particle Accelerator Physics of École Polytechnique Fédérale de Lausanne (EPFL), in Switzerland. This Masters thesis project is completed as part of the exchange year from Imperial College London to EPFL.

All work in this project is done independently of other research in the group. All data are generated using the built-in lattice element models of CERN's MAD-X programme used for simulating beam dynamics inside accelerator lattices. The CERN HTCondor system is used to accelerate the computation process. The Super Proton Synchrotron (SPS) sequence and magnet strength files, as well as other macro files, were provided by Massimo Giovannozzi.

This project is intended to test the feasibility of the novel method of transition crossing, with the goal of being able to test any identified configuration in the real SPS accelerator.

# Contents

<b>1</b>	<b>Introduction</b>	<b>5</b>
<b>2</b>	<b>Background and Theory</b>	<b>6</b>
2.1	Accelerator Physics Fundamentals . . . . .	6
2.1.1	Coordinates . . . . .	6
2.1.2	Circular Accelerators . . . . .	6
2.1.3	Optical Parameters . . . . .	7
2.1.4	Tune, Resonance and Chromaticity . . . . .	8
2.1.5	Emittance . . . . .	9
2.2	Filamentation . . . . .	9
2.3	Momentum Compaction and Transition Energy . . . . .	10
2.3.1	Disturbances at Transition Energy . . . . .	12
2.3.2	Methods of Transition Crossing . . . . .	12
2.4	The SPS Ring . . . . .	14
2.5	The MAD-X Code . . . . .	15
<b>3</b>	<b>Non-linear Beam Dynamics</b>	<b>17</b>
3.1	Magnetic Kick . . . . .	17
3.2	Fixed Points . . . . .	17
3.3	Amplitude-Dependent Detuning and Tune Evaluation . . . . .	18
<b>4</b>	<b>Methods for Configuration Optimisation</b>	<b>21</b>
4.1	Octupole Selection to Minimise Coupling . . . . .	22
4.2	Island Phase and Surface . . . . .	24
4.2.1	Surface Calculation . . . . .	24
4.3	Filementation Test . . . . .	26
4.4	Parameter Scans . . . . .	28
4.4.1	Nominal Chromaticity . . . . .	28
4.4.2	Octupole Strengths . . . . .	28
4.4.3	Horizontal Tune $Q_x$ . . . . .	30
4.4.4	Vertical Tune $Q_y$ . . . . .	34
4.5	Chaos/ Beam Loss . . . . .	34
4.6	Summary of Search . . . . .	34
<b>5</b>	<b>Results and Discussions</b>	<b>39</b>
5.1	Final Identified Configurations . . . . .	39
5.1.1	Maximising $\Delta E_{tr}$ Approach . . . . .	39
5.1.2	Minimising Emittance Growth Approach . . . . .	40



5.2	Uncertainty Analysis . . . . .	43
5.2.1	MAD-X simulations . . . . .	43
5.2.2	Island Surface Uncertainty . . . . .	43
5.2.3	Emittance Uncertainty . . . . .	43
5.2.4	Goodness of Fit . . . . .	43
5.3	Discussions on the Method . . . . .	45
<b>6</b>	<b>Conclusions and Outlook</b>	<b>47</b>
	<b>Acknowledgments</b>	<b>50</b>
	<b>Bibliography</b>	<b>52</b>

# Chapter 1

## Introduction

Particle accelerators are indispensable tools for scientific research, enabling physicists to explore the fundamental building blocks of the universe. They are an essential path to searching for answers to questions about the origin of matter, the nature of forces, and the fundamental laws governing the universe. By colliding charged particles together at very high energies, particle accelerators recreate conditions similar to those that existed just moments after the Big Bang, shedding light onto the early universe. Therefore, they play a crucial role in advancing our understanding of particle physics, nuclear physics, and other related disciplines [1].

The concept of accelerators is simply to apply electromagnetic fields on charged particles to propel them to very high kinetic energy. Complex accelerators are built to push the energy frontiers, achieve higher luminosity, optimise the occupied space, while maintaining the stability of the beam of accelerated particles [2].

However, beam stability can be very easily disturbed. During the acceleration of charged particles in circular accelerators, two opposing effects are experienced as the energy increases: the increase in velocity of the particles, and also the increase of the path length the particle sees due to relativistic effects. Sometimes, they reach an energy known as the transition energy before achieving the desired extraction energy. At the transition energy, these competing effects are equal, and the dominant effect changes from an increase in velocity to an increase in the path length [3]. In literature it can be found that "transition" is short for "transition energy". When the transition energy is crossed, the beam of particles might be severely disrupted in the longitudinal plane (along the direction of beam propagation) due to the increasing path-length effect now dominating. Disruptions in the beam dynamics could potentially yield numerous adverse consequences, including beam losses and a substantial increase in bunch length (length of beam-lets along the longitudinal axis). These effects limit the achievable beam intensity and thus the luminosity of any downstream collision experiments, reducing the statistical power of such experiments.

The existing methods for solving the problem of disturbances at transition energy are discussed in the background section. In this project, a novel method of transition crossing based on Multi-turn Extraction (MTE) [4] is tested by simulating the beam dynamics on the SPS, following from the original proposal in [5], where a proof-of-principle test is simulated on the CERN Proton Synchrotron (PS). The SPS is a more flexible accelerator, and the feasibility is promising. In this project, the method will be tested on a realistic lattice of the SPS with operational constraints imposed.

## Chapter 2

# Background and Theory

This chapter will address the principles of accelerator physics and the prior techniques to overcoming the transition-crossing problem. All momentum, energy, and other computations will be relativistic as the velocity of particles of interest enter the relativistic regime.

## 2.1 Accelerator Physics Fundamentals

### 2.1.1 Coordinates

The curvilinear coordinates  $(x, y, s)$  will be used which correspond to the horizontal, vertical, and longitudinal directions. These form a local reference system as opposed to the global system of Cartesian coordinates  $(X, Y, Z)$ . The coordinate  $s$  is taken as the position along the circular path, measured from a specified start position of the beam line, as shown in Fig. 2.1.

Computation is performed in the 6D phase space, whose points are  $(x, p_x, y, p_y, z, \delta)$  to capture coupling between planes, where the conjugate momenta  $p_x, p_y$  are the derivatives along  $s$  such that  $p_x = dx/ds$ ,  $z = -c\Delta t$  is the negative path length and  $\delta = \Delta E/E_0$  is the fractional energy error where  $\Delta E = E - E_0$ . In this study, the plane of interest is the horizontal transverse plane; hence, the 2D phase space  $(x, p_x)$  is used.

### 2.1.2 Circular Accelerators

Circular accelerators include cyclotrons, betatrons, and synchrotrons. These accelerators consist of a circular path where particles are accelerated to high energies using electromagnetic fields. They are used for a wide range of applications, including high-energy physics research, synchrotron light sources, medical applications, and industrial processes [2]. In contrast to linear accelerators,

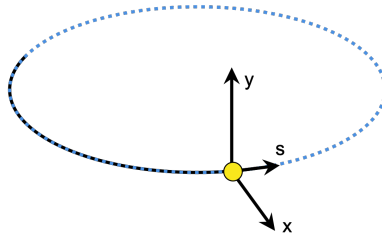


Figure 2.1: Local reference system of a charged particle along its trajectory inside the circular accelerator.

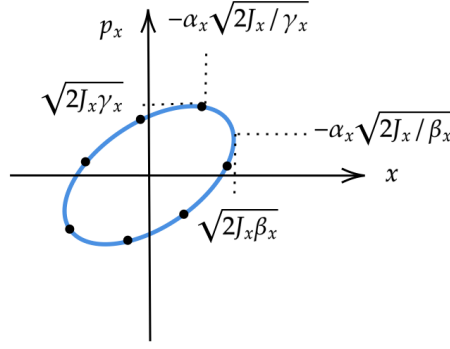


Figure 2.2: Phase-Space ellipse of a particle tracked for many turns at the same point inside the circular accelerator [7].

by continuously orbiting in a ring, charged particles repeatedly receive accelerating voltages to gradually increase the particle energies, which is essential for reaching relativistic energies for fundamental research. The circular design also facilitates the storage and manipulation of the beam. The main elements in these accelerators are:

- Radio-Frequency (RF) cavities which use electromagnetic fields that are synchronous with the frequency of the particle bunches to accelerate them
- Dipole magnets, used to bend and guide the beam
- Quadrupole magnets, used to focus and defocus the beam
- Non-linear magnets such as sextupoles and octupoles to perform corrections [2].

### 2.1.3 Optical Parameters

In a linear machine (one with only dipoles and quadrupoles) with a periodic closed lattice, the beam dynamics is described by the Hill equation [6]. Due to the focusing and defocussing quadrupoles, the analytic solution to Hill's equation shows a pseudo-harmonic oscillation of the beam around the nominal orbit in the transverse plane known as betatron oscillations:

$$x, y(s) = \sqrt{2J_{x,y}\beta_{x,y}(s)} \cos(\phi_{x,y}(s) - \phi_{0,x,y}) \quad (2.1)$$

$$\phi_{x,y}(s) = \int_0^s \frac{ds'}{\beta_{x,y}(s')} \quad (2.2)$$

where  $J$  is the action,  $\phi$  is the phase of the oscillation and  $\beta$  is the betatron function which characterises the amplitude and phase of betatron oscillations. There are two other parameters that characterise the linear dynamics, defined with respect to  $\beta$ :

$$\alpha(s) = -\frac{1}{2} \frac{d\beta(s)}{ds} \quad (2.3)$$

$$\gamma(s) = \frac{1 + \alpha^2}{\beta}. \quad (2.4)$$

Together,  $\alpha, \beta, \gamma$  are known as optical or Twiss parameters.

In phase space, when plotting the  $(x, p_x)$  coordinates of a charged particle at the same longitudinal position after every turn, known as the Poincaré section, a particle with a given initial condition maps out an ellipse of constant action (see Fig. 2.2). However, a more convenient way

to describe the dynamics is using normalised coordinates,  $\hat{x}, \hat{p}_x$ , related to the physical coordinates by the symplectic Courant-Snyder transformation [3]:

$$\hat{x}(s) = \frac{1}{\sqrt{\beta_x(s)}} x(s) \quad (2.5)$$

$$\hat{p}_x(s) = \frac{\alpha_x(s)}{\sqrt{\beta_x(s)}} x(s) + \sqrt{\beta_x(s)} p_x(s). \quad (2.6)$$

This transformation maps the ellipses in physical coordinates into circles and hence can be described by action-angle variables  $(J, \phi)$ , which are the amplitudes and phases (the polar coordinates in this space). The surface of the ellipse, which is the Courant-Snyder invariant, is not changed by transformation, nor it varies when the observation point  $s$  is changed along the ring circumference.

#### 2.1.4 Tune, Resonance and Chromaticity

The tune  $Q_{x,y}$  of a circular accelerator is a measure of the frequency in the transverse plane. This is defined as the number of betatron oscillations per revolution around the ring.

$$Q_{x,y} = \frac{1}{2\pi} \oint \frac{ds}{\beta_{x,y}(s)}. \quad (2.7)$$

When the betatron tune reaches a rational value, resonance is reached and the betatron oscillations amplify. The resonance condition is described by:

$$nQ_x + mQ_y = j, \quad (2.8)$$

where  $n, m$  and  $j$  are integers, and  $|n| + |m|$  is the order of resonance. This project only considers resonances in the horizontal plane, and hence  $m = 0$  is assumed for simplicity. Stable islands are regions of stability with additional fixed points created at resonance by non-linear magnets such as sextupoles and octupoles. The number of islands created is equal to the order of resonance.

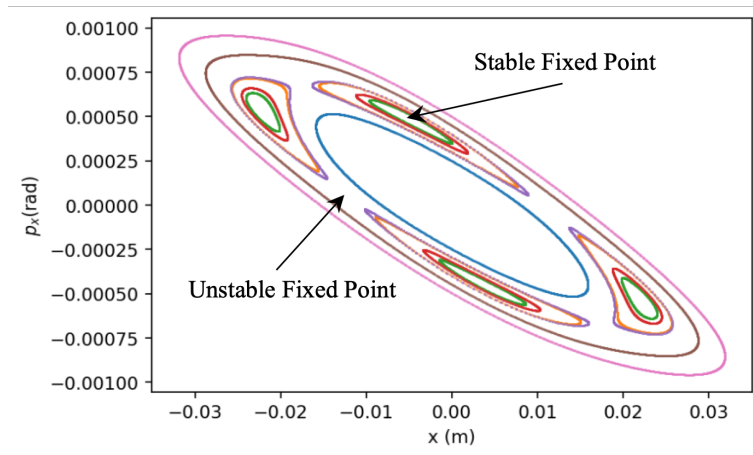


Figure 2.3: Example of a phase space plot of the fourth order resonance for 8 initial conditions tracked. The four additional orbits are at the centre of the four islands created by the octupole. Each orbit is a fixed point.

These islands are regions of phase space where the fractional part of the tune is very close to  $j/n$ . This means that the particle jumps to the next  $j$ -th island anticlockwise after each turn and will return to the original island after  $n$  turns. For example, for the  $1/4$  resonance, the particle

jumps to the next island anticlockwise after 1 turn and returns to the same island after 4 turns. Moreover, these new stable fixed points are closed orbits different from the one centred at the origin and have different optical parameters, as well as different transition energy. As non-linear magnets generate additional stable fixed points, they also generate hyperbolic fixed points that are unstable fixed points. These are the main sources of instabilities, the beam dynamics close to these is chaotic and leads to beam loss. The different fixed points are shown in Fig. 2.3, and the separatrix is the boundary between the different types of particle motion, which in this case is the boundary that divides each island, the central ellipses and the outer ellipses.

When particles have different momenta from that of the reference particle, they will be focused differently by quadrupoles and hence have different tunes [8]. Chromaticity,  $\xi$ , is the ratio between the tune difference from the reference particle and the fractional momentum difference:

$$\Delta Q_{x,y} = \xi_{x,y} \frac{\Delta p}{p_0}. \quad (2.9)$$

The chromaticity will be denoted as  $DQ1$  and  $DQ2$  for the horizontal and vertical chromaticities, respectively, later on in this paper, in accordance with the notation of the simulation tool MAD-X.

The tune and chromaticity are dimensionless.

### 2.1.5 Emittance

The geometric emittance of a beam is a statistical property that describes the spread of particles, and therefore the beam size:

$$\epsilon = \sqrt{\langle x^2 \rangle \langle p_x^2 \rangle - \langle x p_x \rangle^2}. \quad (2.10)$$

The geometric emittance is conserved along  $s$  for a non-accelerating beam. For an accelerating beam, the normalised emittance:

$$\epsilon_n = \beta \gamma \epsilon \quad (2.11)$$

is conserved even during acceleration.

## 2.2 Filamentation

When a beam is injected into a new lattice environment, its emittance would increase if there are errors caused by a mismatch of lattice environments at injection. The main errors include a steering error and a focusing error as shown in Fig. 2.4 and 2.5.

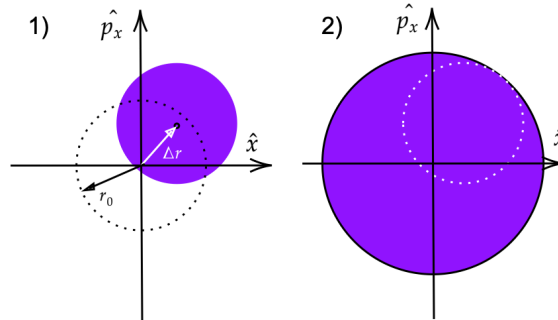


Figure 2.4: Diagram of emittance growth through steering error, the beam rotates around the new fixed point and fills the space.

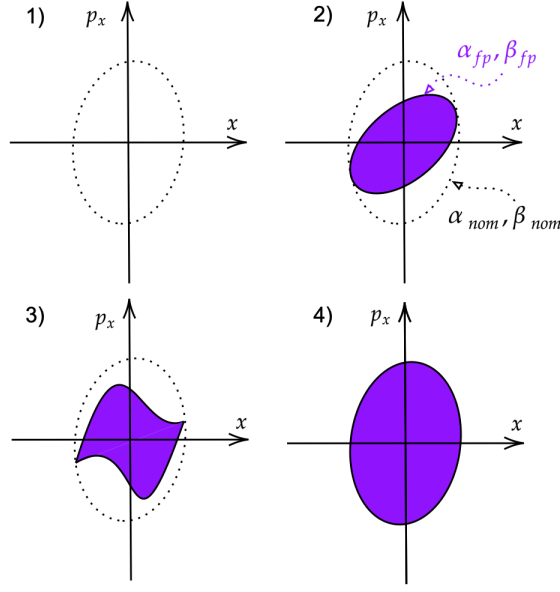


Figure 2.5: Diagram of emittance growth through focusing error, the shape of phase-space ellipse of the injected beam does not match that of the new environment and fills the overlapped space.

The fractional emittance increase due to a steering error is:

$$F_{\text{steering}} = \left(1 + \frac{\Delta r}{r_0}\right)^2 \quad (2.12)$$

where

$$\Delta r = \sqrt{(\Delta \hat{x})^2 + (\Delta \hat{p}_x)^2}; \quad (2.13)$$

where  $\hat{x}$  and  $\hat{p}_x$  are the normalised phase-space coordinates.

The fractional emittance increase due to focusing error is:

$$F_{\text{focusing}} = \frac{1}{2} \left[ \frac{\beta_{\text{nom}}}{\beta_{\text{is}}} + (\alpha_{\text{nom}} - \alpha_{\text{is}})^2 \frac{\beta_{\text{is}}}{\beta_{\text{nom}}} + \frac{\beta_{\text{is}}}{\beta_{\text{nom}}} \right]. \quad (2.14)$$

where the subscript *nom* indicates the nominal orbit and *is* indicates the fixed point of a stable island [9]. Note that  $\alpha$  and  $\beta$  are the previously defined Twiss parameters and not the fine structure constant and relativistic factor.

## 2.3 Momentum Compaction and Transition Energy

The synchronous particle is defined as one with momentum  $p_0$ , it arrives in each radio frequency (RF) cavity at the same phase. Off-momentum particles (with  $p \neq p_0$ ) arrive earlier or later depending on their momentum  $p$ . Their circulation time  $\tau$  is defined as :

$$\frac{\Delta \tau}{\tau} = \left(\alpha_c - \frac{1}{\gamma^2}\right) \frac{\Delta p}{p_0} = \eta \frac{\Delta p}{p_0} \quad (2.15)$$

where  $\gamma$  is the relativistic factor,  $\Delta p$  is the momentum difference from the synchronous particle,  $\eta$  is the slip factor, and  $\alpha_c$  is the momentum compaction factor [10]:

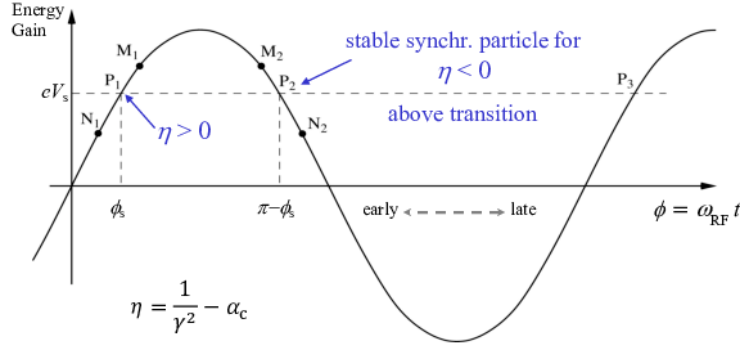


Figure 2.6: Diagram illustrating the energy gained by particles with different momenta. The energy gain is in phase with the RF cavity.  $P$  is the synchronous particle,  $M$  is a particle with larger momentum than the synchronous one, and  $N$  is a particle with lower momentum. The subscript 1 is for the  $\eta > 0$  case and 2 for  $\eta < 0$ . Diagram sourced from [11].

$$\frac{\Delta C}{C} = \alpha_c \frac{\Delta p}{p_0}, \quad (2.16)$$

where  $C$  is the circumference of the circular accelerator, and  $\Delta C$  is the path length change an off-momentum particle sees. The transition energy corresponds to when the circulation time is independent of the momentum offset:

$$\gamma_{\text{tr}} = \frac{1}{\sqrt{\alpha_c}} \quad (2.17)$$

$$E_{\text{tr}} = \gamma_{\text{tr}} m_0 c^2. \quad (2.18)$$

It is important to note that the transition energy can be modified by changing the momentum compaction factor, through controlling the dispersion function  $D$ :

$$\alpha_c = \frac{1}{C} \oint \frac{D(s)}{\rho(s)} ds \quad (2.19)$$

where  $\rho$  is the bending radius [3]. This is the basis for techniques to avoid or safely cross the transition energy.

Equation (2.15) illustrates the counteracting effects of increasing momentum. When the energy is below the transition energy, the slip factor is  $\eta < 0$ . This means that the circulation time of the charged particle is dominated by the effect of increasing velocity, and hence a particle with higher momentum arrives earlier at an RF cavity than the synchronous particle. However, when the energy is above transition,  $\eta > 0$ , the charged particle with higher momentum sees a longer path length. This effect now dominates over the increase in velocity, and hence a higher-momentum particle arrives later than the synchronous particle.

The function of the RF cavity is also to keep the bunches of particles together. Therefore, to focus the particles inside the bunch to ensure stability, the phase of the cavity in which the particle enters must be  $< \pi/2$  below the transition and  $> \pi/2$  above the transition (see Fig. 2.6), and a jump by  $\pi$  of the RF phase should be performed at the transition crossing. The stability is also ensured by the chromaticity. Below transition the higher momenta particle is focused more by quadrupoles and hence the tune is smaller, the chromaticity should be negative. Analogously chromaticity should be positive above transition.



### 2.3.1 Disturbances at Transition Energy

As described above, crossing the transition energy can cause numerous adverse effects. One such disruption arises from instabilities that arise within the longitudinal plane. In this plane, the beam is divided into equal bunches where particles oscillate longitudinally around the synchronous particle, a phenomenon called synchrotron motion. The stable region that accommodates the particles is called a bucket. Near the transition energy, synchrotron oscillations lose adiabaticity and as a result the bucket length is rapidly modified. Consequently, the momentum spread of particles may exceed the momentum aperture of the bucket, potentially leading to beam losses [3].

All particles in the beam do not cross transition at the same time either. The transition energy crossing time of each particle is actually dependent on their individual momenta. The momentum spread of the bunch therefore leads to a range of transition energies, causing the particle to cross transition at different times.

Furthermore, particles within a bunch exert electromagnetic forces on one another, known as space-charge effects. They introduce a bunch length mismatch at the transition point, causing instabilities. Below the transition, the space charge is a defocusing effect, thus increasing the bunch length; and above transition, a focusing effect and hence decreases the bunch length. Therefore, there is a mismatch in the equilibrium length of the bunch above and below the transition that causes the length of the bunch to oscillate. This causes the growth of the emittance in the longitudinal plane [12].

### 2.3.2 Methods of Transition Crossing

While it is preferential to design an accelerator with a transition energy outside the machine's energy range, or even without a transition energy at all (imaginary-gamma scheme), this is not always feasible due to the complexity of the optics involved [13, 14]. Therefore, mitigation measures are implemented to cross the transition energy minimising instabilities and beam losses. The main transition-crossing method in use is the gamma-jump scheme.

#### Gamma Jump Scheme

This approach was first implemented in the CERN PS to accelerate protons through transition up to 25 GeV. The gamma-jump scheme involves using fast-pulsing quadrupoles at locations of non-zero dispersion. As seen in Eq. (2.19), this enables control of the momentum compaction, and hence the transition energy of the lattice. By pulsing the current inside these quadrupoles before the energy reaches the transition energy, it is possible to rapidly reduce the transition energy to below the beam energy, hence artificially crossing the transition, and then subsequently returning to the unperturbed transition energy. The pulsing of the quadrupoles is synchronised with the arrival of particles, and therefore the period is 2.1  $\mu s$  - the revolution time in the PS. This transition-crossing rate is much faster than the rate of increase of the particle energies. Further progress is made where  $\pi$ -doublets (pairs of quadrupoles that are separated by a phase advance of  $\pi$ ) are used to minimise the tune shift caused by changing the quadrupole strengths. More details on the gamma-jump scheme and modifications can be found in [12] and [10]. This method is now in regular use at the CERN PS.

#### Imaginary or Infinite Gamma Schemes

It is possible to eliminate the transition energy from the lattice by using a negative momentum compaction factor, as seen in Eq. (2.17), which results in the transition energy becoming imaginary

[15]. Achieving this increases the complexity in lattice design. In Eq. (2.19), it is shown that to render the momentum compaction negative, the averaged dispersion function must be negative. This can be accomplished by incorporating reverse bends into the lattice [14]. Another approach is to insert multiple straight sections with a  $\pi$  phase advance and a few reverse bends, which leads to net zero dispersion and infinite transition energy [13, 14]. However, these manipulations cause changes to the original tune, necessitating additional measures for compensation.

To ensure the stability and performance of the accelerator, the method is also highly constrained by requirements on preserving the betatron phase advance and the beta functions, as well as zero dispersion in the straight sections. Thus, additional consideration must be given to the lattice design. Examples of lattice designs that achieve these objectives can be found in [15, 16]. Additionally, the Low Energy Antiproton Ring (LEAR), now the Low Energy Ion Ring (LEIR) at CERN, also utilises these techniques [17]. The effects and implications of these lattice manipulations are discussed in detail in [14].

### Transition Crossing using Stable Islands

To further improve transition crossing techniques, a novel approach inspired by Multi-Turn-Extraction (MTE) [4] was introduced [5]. MTE uses the principles of creating stable islands at resonance by non-linear magnets described in Subsection 2.1.4. The goal is to overcome the problem of beam losses at the electrostatic septum during beam extraction from the accelerator. The MTE technique starts by intentionally operating the accelerator close to a resonant horizontal tune. The tune is gradually shifted towards the resonance point in an adiabatic manner using non-linear magnets like sextupoles and octupoles. As the tune is swept through resonance, islands of stability are created in the centre of phase space and trap particles within them, generating beam-lets. As the tune is swept further, the islands, along with the trapped particles, move outward so that they are far apart enough so that the blade of the septum can intercept one beam-let at a time and extract the beam-let. As the periodicity  $n$  of the islands is equal to the order of resonance, the beam-lets can be extracted individually over  $n$  or  $n + 1$  turns depending on whether the centre remains populated [18]. A study of the different resonances to be used in MTE is explored in [19], and the approach could already be transformed to solve other problems, such as the reverse process of multi-turn injection in [20]. This approach has been used successfully, such as at the CERN PS [21] and shows that the use of stable islands is based on solid foundations.

To apply this principle to transition crossing, the islands are generated using the same principle. However, instead of creating islands in the process of sweeping the tune, the tune is kept constant and islands would be present since injection but unpopulated. These islands are additional stable regions in phase space that the beam can be kicked into and have transition energies distinctly different from that of the central region (nominal fixed point). Note that all islands have the same transition energy. Moreover, the creation of these islands has minimal disturbances to the optics at the nominal fixed point, and hence the tune shift introduced by the previous schemes is no longer an issue.

A dipolar kicker is used to kick the beam from the nominal fixed point to an island and back. There are hence two transition energies in this setup (of nominal fixed point or of the island), and a kick process can be designed to choose the environment so as to choose which transition energy it experiences. There are two possible scenarios, as the island transition energy can be below or above that of the nominal. Figure 2.7 illustrates the kick process for the two scenarios.

The concept behind this approach is to kick the beam into a stable island prior to reaching the original (nominal) transition energy, accelerate within the island until the original transition

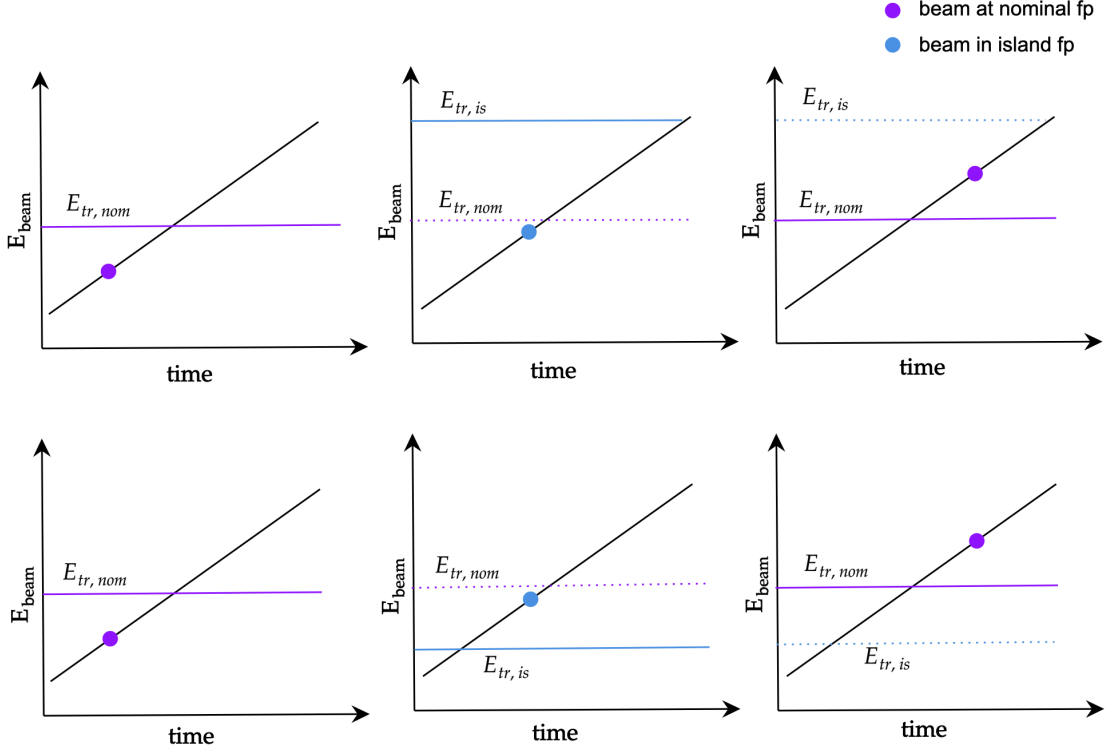


Figure 2.7: The novel transition crossing scheme. Top: where  $E_{tr,nom} < E_{tr,is}$ , the beam is kicked back to the nominal orbit before reaching the island transition energy. Bottom: where  $E_{tr,nom} > E_{tr,is}$ , there is no constraint on the maximum energy reached inside the island but the beam is kicked into the island after passing the island transition energy.

is crossed, and subsequently return the beam to its original orbit with energy is already above the transition energy; effectively having avoided crossing transition, see Fig. 2.7. To validate this approach, a proof-of-principle simulation was conducted on a lattice derived from that of the CERN PS. Remarkably, the results demonstrated high effectiveness with a minimal increase of less than 10% in the emittance for both transverse planes and no beam losses [5]. Encouraged by these promising findings, the next step involves numerical simulation of the beam with application of the method on a realistic lattice of the CERN SPS to assess its feasibility, which is the aim of this project.

## 2.4 The SPS Ring

The Super Proton Synchrotron (SPS) is the second-highest energy machine at CERN. As part of the accelerator complex, hydrogen anions ( $H^-$ ) are first generated from the hydrogen gas and accelerated in Linear Accelerator 4 (LINAC4). They are taken by the Proton Synchrotron Booster (PSB) where they are stripped of the electrons during injection and become a proton beam and accelerated to a kinetic energy of 2 GeV. They are then transferred through CERN's accelerator chain with several circular machines, such as the PS and the SPS, where they are further accelerated before being injected into the LHC for collider experiments or sent to one of the many fixed target experiments located at CERN [23]. The general layout of the accelerator complex is shown in Fig. 2.8.

## The CERN accelerator complex *Complexe des accélérateurs du CERN*

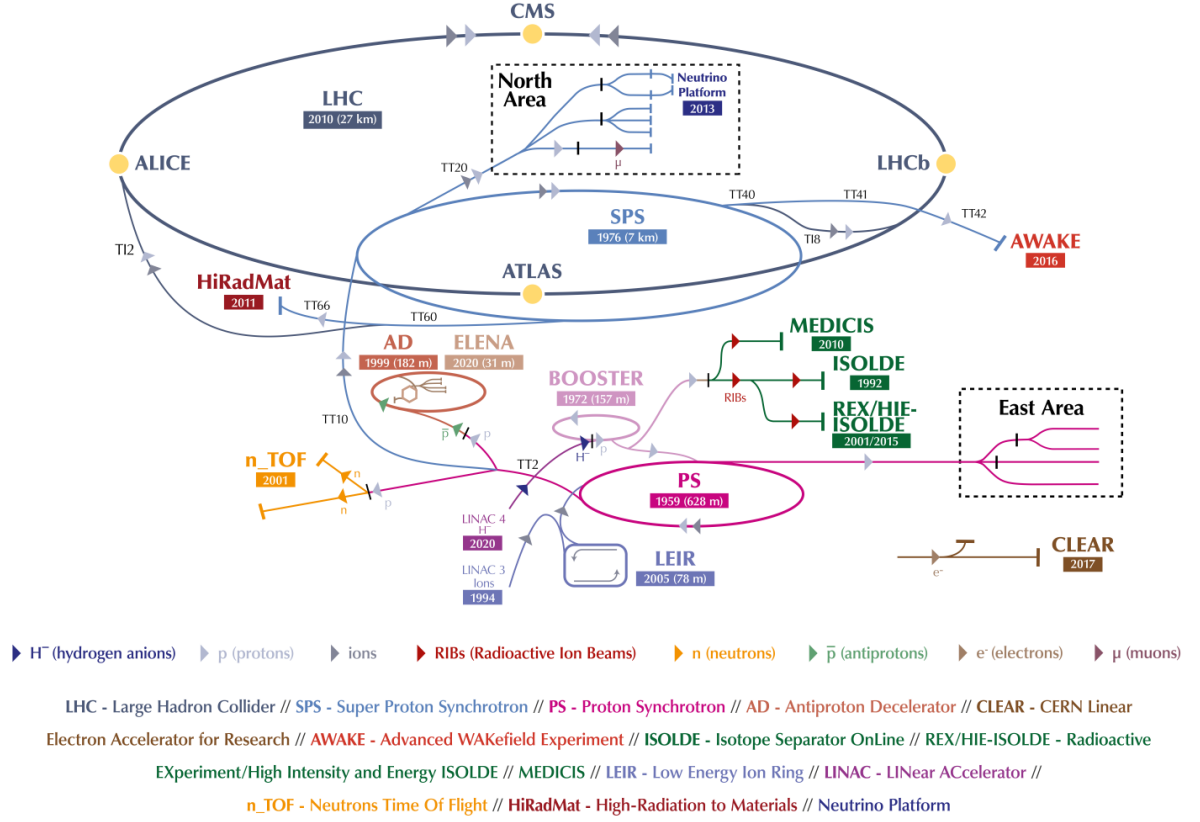


Figure 2.8: A diagram of the CERN accelerator complex, with the LHC and its injectors [22]

The SPS has a circumference of 6.9 km, and is designed to accelerate protons of energy from 26 GeV to 450 GeV to inject beams into the LHC and from 14 GeV to 400 GeV for beams for fixed target experiments. Transition is only crossed when beams are injected at 14 GeV.

The SPS includes the following main magnets for beam manipulation:

- 744 dipoles
- 216 quadrupoles
- 118 sextupoles
- 68 octupoles

Together these magnets form 108 periodic cells and 6 superperiods which are repetition of groups of periodic cells [24].

## 2.5 The MAD-X Code

MAD-X (Methodical Accelerator Design) [25] is the code used in this project to track particles and calculate their optical parameters, as well as relevant quantities such as chromaticity in the horizontal and vertical directions ( $DQ1$ ,  $DQ2$ ), fixed point positions, and transition energies. The

Polymorphic Tracking Code (PTC) module is the most accurate single-particle tracking tool available. It is a symplectic integrator, which means that it uses the exact Hamiltonian to maintain accuracy; hence, it does not truncate higher-order terms. It also includes tools such as normal forms to accurately simulate the effects of non-linear elements, and can capture the non-linear perturbations caused. The thickness of the elements is preserved and considers the field distribution within the element. Tracking is done by using element-wise transfer maps that describe the linear and non-linear effects based on properties of the elements, such as magnetic field strengths, pole shapes, and beam parameters [26]. The main PTC functions used in the project are PTC Track which tracks the turn-by-turn position of the particle, and PTC Twiss which computes the Twiss parameters,  $\gamma_{\text{tr}}$ , chromaticities, fixed point position, and others.

## Chapter 3

# Non-linear Beam Dynamics

Non-linear dynamics studies the effects of non-linear magnets on the beam dynamics. Normal Forms theory [27] is the generalisation of the Courant-Snyder transformation to non-linear dynamics, and much can be understood about the control of islands through this. However, the kick that is performed in this project is only a change of  $p_x$  which is in physical coordinates; hence, later analysis of the islands still have to be in physical coordinates  $(x, p_x)$ .

### 3.1 Magnetic Kick

For lattices with only normal magnets (magnets with magnetic field perpendicular to the beam's longitudinal axis) and no skewed magnets (rotated magnets that have a tilted magnetic field with respect to the longitudinal axis), the change in transverse momentum a particle experiences is expressed as:

$$\Delta p_x - i\Delta p_y = - \sum_{n=0}^{\infty} k_n \frac{(x + iy)^n}{n!} \quad (3.1)$$

where  $k_n$  is the multipole coefficient of normal magnets, or later referred to as the magnet strength, defined as :

$$k_n = \frac{1}{B\rho} \frac{\partial^n}{\partial x^n} B_y, \quad (3.2)$$

where  $B_y$  is the vertical magnetic field strength and  $B\rho$  is the magnetic rigidity of the particle. Eq. (3.1) is used to form the 4D symplectic one-turn map in Normal Forms:

$$\begin{pmatrix} \hat{x} \\ \hat{p}_x \\ \hat{y} \\ \hat{p}_y \end{pmatrix}_{n+1} = R(\omega_x, \omega_y) \begin{pmatrix} \hat{x} \\ \hat{p}_x + \sqrt{\beta_x} \Delta p_x \\ \hat{y} \\ \hat{p}_y + \sqrt{\beta_y} \Delta p_y \end{pmatrix}_n \quad (3.3)$$

where  $R(\omega_x, \omega_y)$  is a rotation matrix (see [19]), and  $\omega_{x,y} = 2\pi Q_{x,y}$ .

### 3.2 Fixed Points

In Normal Form Coordinates [27], the phase-space curves are again mapped to circles of radius  $\rho$ , defined as :

$$\rho = x^2 + p_x^2 + \text{higher-order terms.} \quad (3.4)$$

It is easier to describe non-linear motion in Normal Forms. From Eq. (3.3), and assuming a tune close to a rational (resonant) one, the Hamiltonian in terms of  $(\rho, \theta)$ , the action angle variables is:

$$H = 2\pi Q_x \rho - \frac{\Omega_2}{2} \rho^2 - R(\theta) \rho^2 + O(\rho^3) \quad (3.5)$$

where  $R(\theta)$  is the resonant function [28] and the angular dependence produces the fixed points.  $\Omega_2$  is the amplitude-dependent detuning coefficient, defined as:

$$\Omega_2 = -\frac{1}{16} \sum_l k_{3,l} \beta_{x,l}^2 + F(\beta_x, \phi_x, k_2). \quad (3.6)$$

where  $l$  runs over all octupoles used in the lattice,  $k_{3,l}$  is the octupole strength of each,  $F$  is a quadratic function of  $k_2$ , the sextupole strengths, with coefficients dependent on  $\beta_x$ , and  $\phi_x$  with more details and derivations found in [28].

These equations give relations of the non-linear tune:

$$\nu_x = \frac{1}{2\pi} \left\langle \frac{\partial H}{\partial \rho} \right\rangle_\theta = Q_x - \frac{\Omega_2}{2\pi} \rho - \frac{\langle R(\theta) \rangle}{\pi} \rho. \quad (3.7)$$

When the non-linear tune reaches a resonant value, fixed points emerge. Hence the amplitude of fixed points in Normal Forms coordinates is :

$$\rho^*(\Delta, \Omega_2) = \frac{2\pi\Delta}{\Omega_2 + 2\langle R \rangle_\theta} \approx \frac{2\pi\Delta}{\Omega_2} + O(\Delta^2), \quad (3.8)$$

where  $\Delta = Q_x - \bar{Q}_x$ , is the difference of the starting (linear) tune to the resonant tune reached by non-linear effects. This equation shows that to control the fixed points,  $\Delta$  is changed by defining different starting tunes  $Q_x$ , and  $\Omega_2$  is changed by using different  $k_3$  values, the octupole strengths. Therefore,  $Q_x$  and  $k_3$  can be used to change the position of the fixed point, and hence the surface of the islands. The  $F$  in Eq. (3.6) is negative number, and is dominating in most octupoles in the SPS, depending on the configuration. This means that an increase of the non-linear tune regardless of the sign of  $k_3$ , thus resonance can be reached with any small  $k_3$ . The only difference is that a negative  $k_3$  will add to the effect of  $F$ , and a positive  $k_3$  will reduce the effect  $F$ ; hence negative strengths give larger islands. From Eq. (3.8), for larger islands (all islands have the same surface), one should increase  $|k_3|$ ; and for islands further away from the origin, one should increase  $|Q_x - \bar{Q}_x|$  if  $k_3$  is positive, and vice versa. It is interesting to note that it is possible to keep an island fixed point at the same position in phase-space, while changing the surface of islands. One can then use this to construct a configuration where the centre region and islands have approximately the same surface.

### 3.3 Amplitude-Dependent Detuning and Tune Evaluation

As seen in Eq. (3.7), non-linear effects alter the tune of each particle so that the tune depends on the amplitude  $\rho$ , a phenomenon known as amplitude-dependent detuning. This is analogous to the scenario of a pendulum with large displacements where the frequency of the swing is no longer constant and depends on the initial displacement.

To evaluate the tune for each particle, a special technique derived from Normal Form theory is used [29]. As the physical coordinates  $(x, p_x)$  of the particle are tracked at each turn at the same position along the orbit, a Fourier Transform can be performed on these to estimate a tune. This is done by using the complex normalised coordinate  $z = \hat{x} - i\hat{p}_x$  so that  $z$  rotates around the

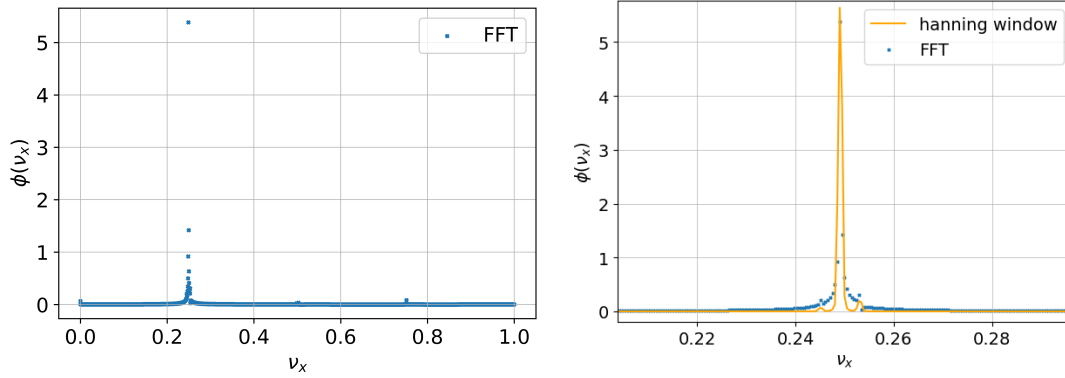


Figure 3.1: Left: the frequency spectrum by taking the Fourier transform of  $z$ , the complex normalised coordinate of the tracked particle. Right: Comparison of just the Fourier transform and the Fourier transform after applying the Hanning window to the complex coordinates, zoomed in around the main peak.

circle in phase space at the frequency of the non-linear tune  $\nu_x$ . However, the resolution hence accuracy of this is entirely reliant on the number of turns tracked. For a simple tracking task without the need to calculate the island surface, 2048 turns are used, which gives a tune resolution of only  $1/2048$ . The frequency spectrum is shown in the left-hand graph in Fig. 3.1, where a primary peak, representing the particle tune, is visible. Smaller secondary peaks, known as side bands, are also visible. It is clear that, because of the data spacing, the highest point on the peak might not correspond to the centre of the peak, thus the actual tune. Figure 3.2 shows that when calculating the tune of particles of different actions, the low resolution of the fast Fourier Transform (FFT) method gives steps within the tune. Indeed, this resolution scales with the number of turns tracked, but tracking is a time-consuming process, and it would be beneficial to improve the resolution without tracking for longer.

To solve this problem, an interpolation method is developed in [30] and discussed in [29], the key aspects employed in this analysis are summarised here. The interpolation method was tested using the 4D Henon map [29] to model the beam dynamics. The interpolated tune is calculated from the two highest points in the main peak:

$$\nu = \frac{k}{N} + \frac{1}{\pi} \arctan\left(\frac{|\phi(\nu_{k+1})| \sin(\pi/N)}{|\phi(\nu_k)| + |\phi(\nu_{k+1})| \cos(\pi/N)}\right), \quad (3.9)$$

where  $k, k+1$  are the indices of the two highest points in the main peak,  $N$  is the number of coordinates, which is the number of turns tracked, and  $\phi$  is the amplitude at each frequency.

This interpolation improves the calculated tune to have an error proportional to  $1/N^2$ . However this can be improved further with a data windowing method that uses the Hanning filter to put weights  $\chi(n)$  on each input data point  $z(n)$  with index  $n$  before the FFT such that:

$$\phi(\nu_j) = \frac{1}{N} \sum_{n=1}^N z(n) \chi(n) \exp(-2\pi i n \nu_j), \quad (3.10)$$

and

$$\chi(n) = 2 \sin^2\left(\frac{\pi n}{N}\right). \quad (3.11)$$

The Hanning filter accentuates the main peak while damping the secondary peaks. With this filter,



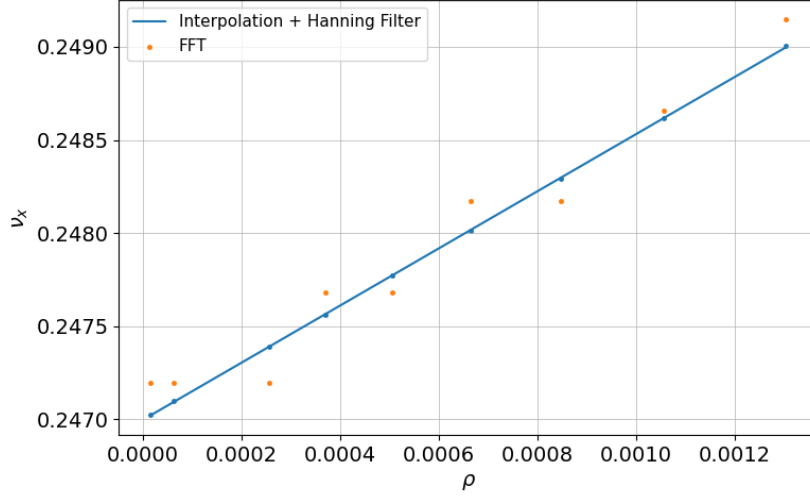


Figure 3.2: Comparison of the tune calculated using just the FFT and with the interpolation method with the Hanning Filter.

the interpolated tune is now :

$$\nu = \frac{k}{N} + \frac{1}{2\pi} \arcsin \left[ A \left( |\phi(\nu_k)|, |\phi(\nu_{k+1})|, \cos\left(\frac{2\pi}{N}\right) \right) \sin \frac{2\pi}{N} \right], \quad (3.12)$$

where the function A is:

$$A(a, b, c) = \frac{-(a + bc)(a - b) + b\sqrt{c^2(a + b)^2 - 2ab(2c^2 - c - 1)}}{a^2 + b^2 + 2abc}. \quad (3.13)$$

This results in a final error scaling as  $1/N^4$ . The calculated tune using the interpolation method with data filtering is compared to the simple Fourier Transform method in Fig. 3.2. The tune calculated this way follows very closely to a straight line with  $\rho = x^2 + p_x^2$ , which is predicted in Eq. (3.7). Therefore, for the number of turns used in this project, which are all at least 2048 turns, the tune error is of the order  $10^{-14}$  which is negligible.

It is also important to note that the FFT function in the Python numpy module works much more efficiently for a turn number that is a power of 2, hence the choice of number of turns tracked throughout this project [31].

## Chapter 4

# Methods for Configuration Optimisation

The novel transition crossing method described in Subsection 2.3.2 is to be tested on the SPS and hence an optimum magnet setup must be identified to generate islands that can accommodate the beam during the kick process. The islands need to satisfy a number of constraints to avoid beam loss and significant disturbance, and most importantly, to successfully cross transition. There is only one dipolar kicker in the SPS (MKQH) that can be used to kick the beam into the island and back [32]. The kicker displaces the beam by giving every particle the same change in horizontal momentum  $p_x$ . The main constraints of the octupole setup configuration are as follows:

- Island phase – at the  $s$  position of the kicker, the  $x$ -coordinate of the island should be as close to 0 as possible, to ensure that the entire beam can be kicked into the island, and to minimise filamentation from steering error.
- Island surface – islands as well as the centre stable region must be large enough to accommodate the entire beam of normalised emittance around 1 mm mrad, a standard beam at the SPS.
- Transition energy – islands must have a transition energy at least 0.5 GeV different from the nominal transition energy to avoid disruptive effects near transition.
- Island optics – at the position of the kicker, the optical parameters inside islands should be as similar to that at the nominal fixed point as possible to minimise filamentation from focusing errors.
- Chromaticity – to avoid the development of head-tail instabilities, the value of chromaticity at the centre and inside the island should be negative in both the  $x$  and  $y$  directions below transition, and positive above transition [8].
- Coupling – coupling to the vertical and longitudinal planes must be minimised.

In this method a fourth-order resonance created by octupoles is chosen due to its symmetry: at the location of the kicker, it is possible to have an island just above the central (nominal) fixed point and one just below. This means if the dipolar kicker displaces the beam into the top island, it can be kicked back to the origin after acceleration when it has reached the bottom island, thus only one direction of the kick is needed. Higher-order resonances are not considered as the islands become smaller with increasing resonance order. In addition, octupoles generate islands

without disturbance to the chromaticities at the nominal fixed point; hence, the use of sextupoles to generate islands should be avoided if octupoles provide a good enough configuration so as to more easily control the chromaticities.

As chromaticities need to be negative below transition and positive above, a chromaticity jump is needed, and hence two configurations should be envisaged. The two configurations would need islands at the same position in phase space to minimise filamentation during the switch of the configurations at the chromaticity jump. The switch will be performed when the beam has been kicked into an island, by changing the octupole and sextupole strengths. As the change can be done just after kicking into an island or just before kicking back to the centre, only one of these configurations requires the chromaticity constraint imposed.

## 4.1 Octupole Selection to Minimise Coupling

The octupole(s) with an optimal strength will be identified to best satisfy all constraints. There are a total of 68 octupoles in the SPS, categorised into 4 types: Landau Damping (LOD), Extraction (LOE), Extraction New (LOEN) and Focusing (LOF). First, octupoles are selected to minimise coupling. The LOE, LOEN and LOF octupoles are all placed at locations of high  $\beta_x$  and low  $\beta_y$ . These satisfy the constraint of minimising the disturbance to the vertical plane. The following equation illustrates the coupling of the planes due to octupoles:

$$\begin{pmatrix} \hat{y} \\ \hat{p}_y \end{pmatrix}_{n+1} = R(\omega_y) \begin{pmatrix} \hat{y} \\ \hat{p}_y + -\frac{k_3}{6}\beta_y(\beta_y\hat{y}^3 - 3\beta_x\hat{x}^2\hat{y}) \end{pmatrix}_n \quad (4.1)$$

which is derived from Eqs. (3.1) and (3.3) (more details in [19]). The octupole perturbations in the horizontal plane ( $\hat{x}$ ) are coupled to the vertical plane ( $\hat{y}_{n+1}, \hat{p}_{y_{n+1}}$ ) but can be controlled by a single parameter  $\beta_y$ . In fact, it has been proven that the coupling can be safely neglected if  $\beta_y$  is small [4]. The dispersion function plays a key role in the longitudinal dynamics, as shown in Eq. (2.19). The dispersion couples the transverse ( $s$ ) and longitudinal ( $\alpha_c$ ) motions. Placement of the non-linear magnet at a position of low dispersion is thus needed to not alter the original momentum compaction factor. In addition, as understood in the studies of MTE [28], dispersion introduces chromatic aberrations. Hence, choosing to introduce the non-linear effects in regions of zero dispersion allows differentiation of chromatic and non-chromatic effects and hence control the islands more easily.

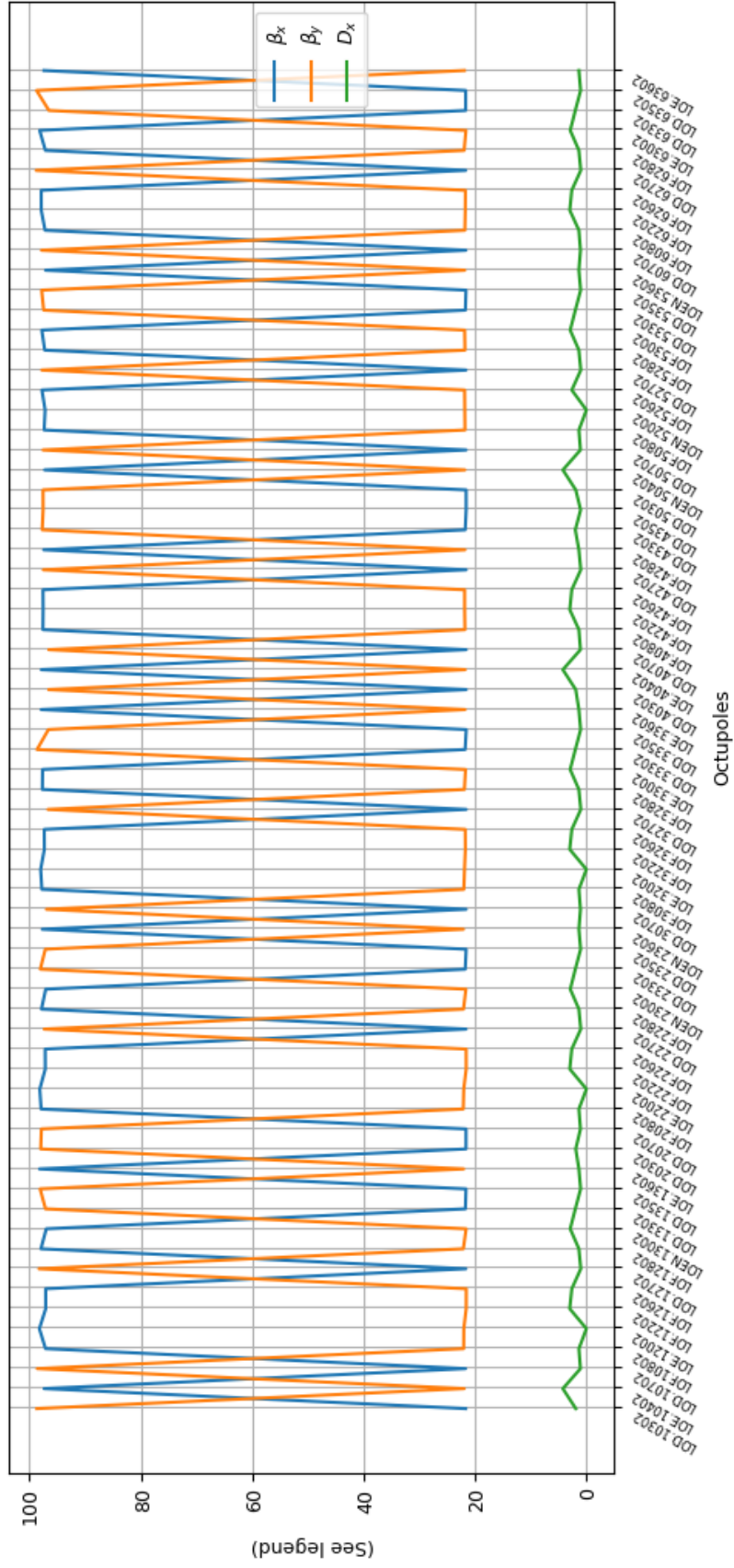


Figure 4.1: Plot of the horizontal and vertical beta functions as well as the horizontal dispersion at locations of octupoles. The vertical dispersion is always 0 as dispersion only come from dipoles that bend the beam in the horizontal direction, hence is not shown. Octupoles are ordered as they appear in the SPS. Note that the lines between vertices are simply to guide the eye and not an indication of the variation of optical parameters between each octupole.

A summary plot of the beta functions and dispersion at the location of all octupoles in the SPS is shown in Fig. 4.1. Four octupoles are identified that simultaneously satisfy high  $\beta_x$ , low  $\beta_y$ , and low dispersions. They are LOE.12002, LOE.22002, LOE.32002, and LOEN.52002.

## 4.2 Island Phase and Surface

Particles are tracked over 2048 turns using MAD-X for a range of initial conditions to trace the Poincaré sections. 2048 turns suffice for simple inspection of the Poincaré section. PTC Track is used to model the real lattice with thick magnets and is done for all combinations of the 4 octupoles identified, i.e. with single octupoles, pairs, triplets and all 4 octupoles switched on. The Poincaré sections are analysed along with the results from PTC Twiss, which gives the fixed point positions for each configuration. To investigate island properties, PTC Twiss is run for a lattice 4 times the SPS lattice. This is required to converge on a fixed point in a closed orbit of periodicity 4, the periodicity of the octupole-generated islands. An initial guess of the fixed point position must be provided to PTC twiss for convergence. It is necessary to check the fixed point position by tracking a few particle trajectories to see if it converged to the correct point.

Both positive and negative strengths of the octupoles are investigated. For a good starting point, the linear tune  $Q_x$  is set to 26.747, just below the 3/4 resonance; and the octupole strengths used are all  $0.6 \text{ m}^{-4}$ . With this starting point, configurations with fixed point  $|x| < 0.01\text{m}$  are marked for further study.

For negative octupole strengths, the island phase is offset by  $45^\circ$  with respect to the positive octupole. Negative strengths are also found to give larger islands than those generated using positive strengths (as explained in Chapter 3). For the standard SPS beam size, only negative strengths give large enough islands, and hence only negative strengths are investigated after this observation.

### 4.2.1 Surface Calculation

#### Tune Method

The "surface" of an island refers to the area of the stable region in phase-space. The island surface must be evaluated to determine whether a beam fits inside.

As MAD-X does not have a function to converge to the separatrix, this has to be done manually to estimate the surface of islands. A dense grid of initial conditions that covers the entire island is tracked. Then the tune is calculated for each point. The stable region (island) should be where the tune is very close to 0.75. However, closer to the separatrix, due to the chaotic motion, the interpolation method for tune evaluation breaks down and the calculated tune has larger errors. Hence, a tolerance level for the difference from 0.75 was found to accommodate for the error near the separatrix.

Through careful comparison of the tolerance level with the tracked trajectory, a tolerance of 0.0003 is chosen for the grid of 7800 particles spanning a total surface of 89 mm mrad in phase-space. Figure 4.2 also shows that 0.0003 is just before the calculated surface rising steeply. Then the surface is estimated by:

$$\text{surface} = \frac{\text{no. of points inside island}}{\text{total no. of points}} \text{total surface of tracked grid.} \quad (4.2)$$

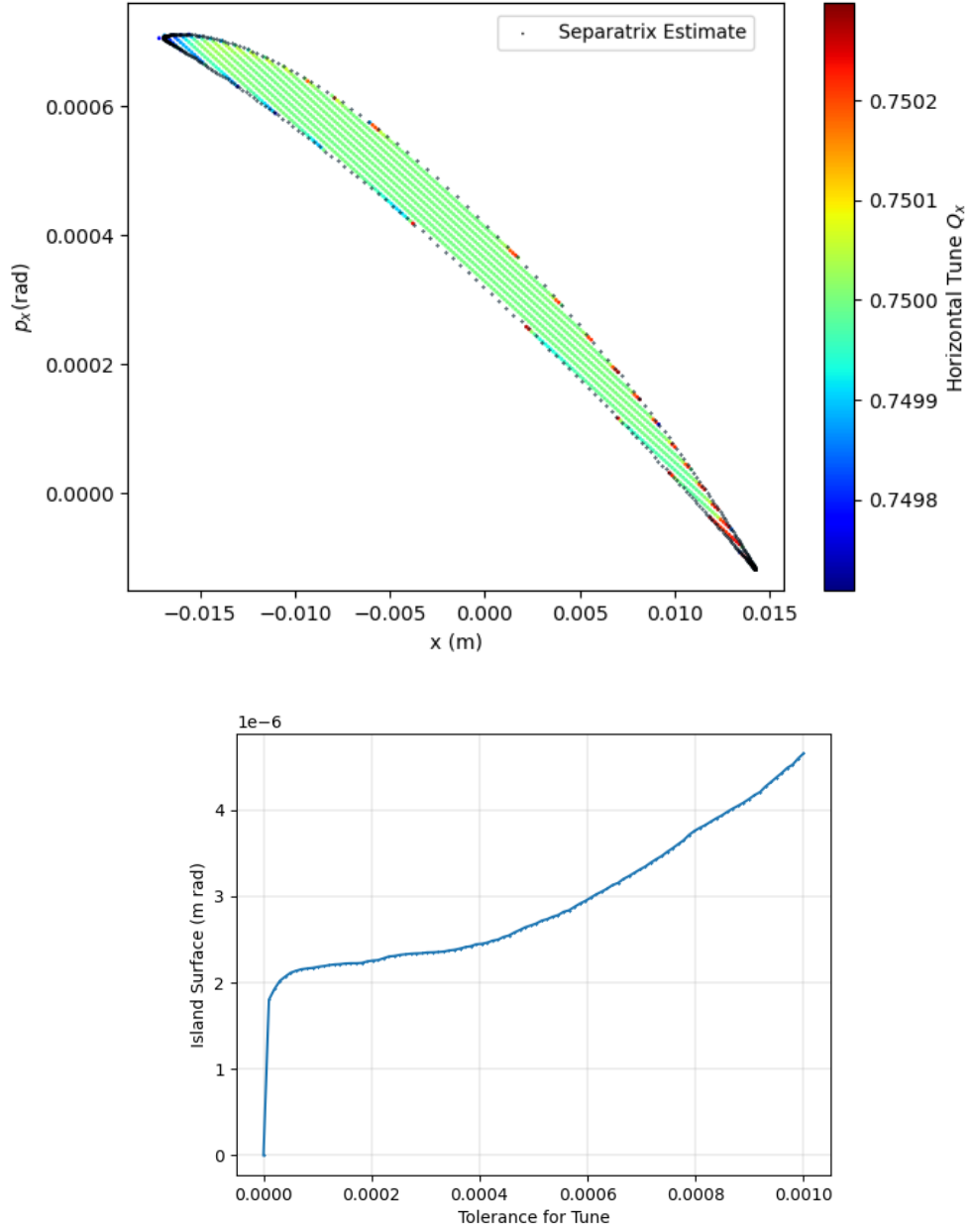


Figure 4.2: Top: Result of surface calculation using the tune of each initial condition tracked using a tolerance of 0.0003. The black border is the result of the separatrix estimate overlaid on the plot. Bottom: Surface calculated versus the set tolerance for the tune. Above the 0.0003 tolerance level, the line begins to rise steeply and is when the the method captures points outside the island.

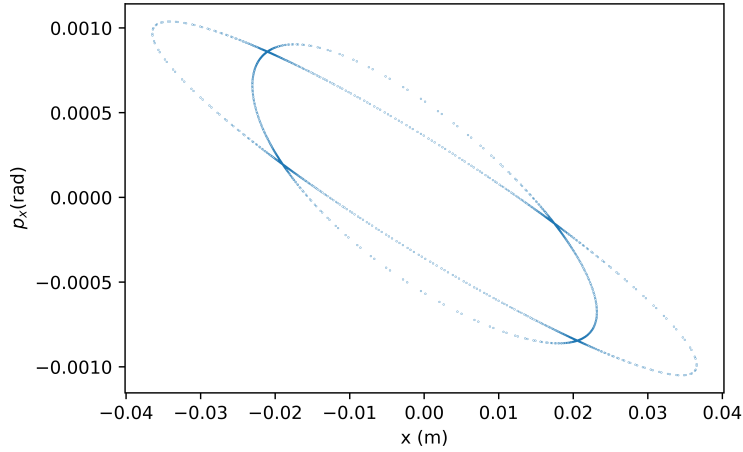


Figure 4.3: Tracking of the orbit closest to the separatrix. This orbit is identified to calculate the surface of the island.

### Separatrix Method

Another method of estimating the island surface is identified. By using a smaller grid of initial conditions close to the unstable fixed point, one can again use the tune to select a range of initial conditions whose orbits are close to the separatrix, and narrow down the range by inspection until the closest is found. Then the surface is numerically estimated by slicing the surface into triangles from the centre. This is shown in Fig. 4.3.

### Method Comparison

Comparing the two surface estimation methods, one can see that although the tune method has captured a surface that overlaps very well with that of the separatrix method in 4.2, the result is highly dependent on the choice of tolerance and there is no sharp boundary to decide this tolerance level. At a tolerance of 0.0003, the area estimated has a 2.6% difference with that calculated with the separatrix method. Moreover, the separatrix method requires much fewer data points to track but has the same density of points. Therefore, the separatrix method is chosen to calculate island surfaces.

## 4.3 Filamentation Test

The equations for the emittance growth, Eqs. (2.12) and (2.14) describe a linear system and give a good estimate of the growth. To include the effects of filamentation from non-linear magnets, this analytic treatment is insufficient. There will be more deviations for larger beams, as particles are farther away from the fixed point. To find the emittance (and emittance growth), numerical simulations are required, tracking a large number of particles. To do this efficiently, instead of tracking a beam of a set number of particles, a dense grid of initial conditions can be tracked and any beam distribution within the grid can then be calculated using appropriate weights. Like the Poincaré section of a single particle, a beam in phase-space also has an elliptical distribution, which has a 2D Gaussian shape in normalised coordinates. Hence to simulate this, each initial condition in the tracked grid is given a 2D gaussian weight in normalised coordinates, with the specified beam size and position, and then transformed back into physical coordinates. The emittance is calculated using these weights at the end of the tracking to measure the emittance growth. When

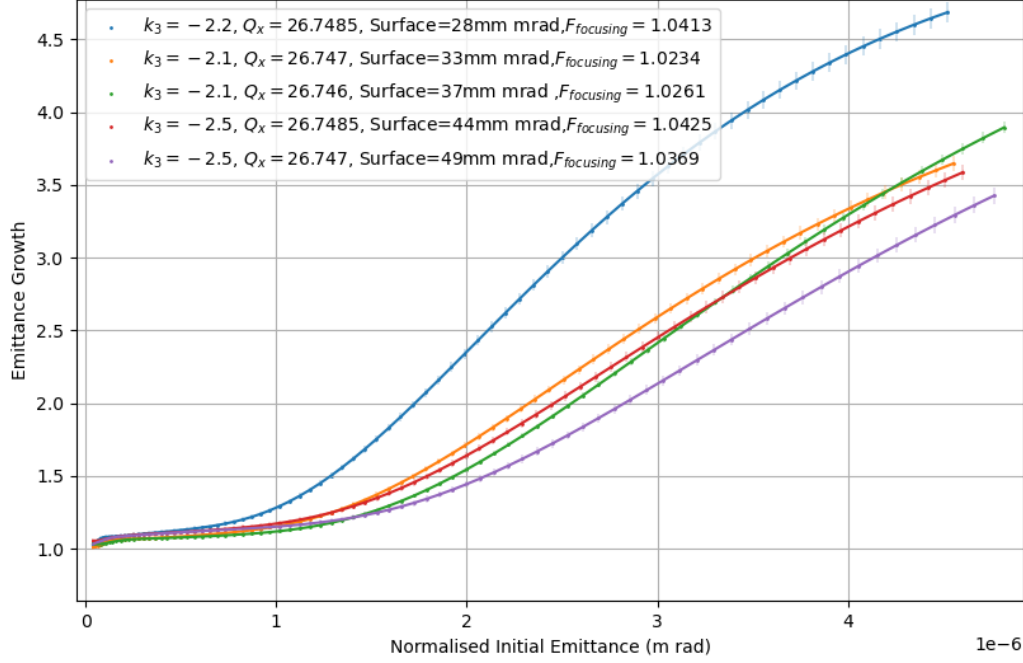


Figure 4.4: Emittance growth (final emittance/initial emittance) of a beam that has just kicked into an island, as a function of the initial normalised emittance. The larger the original beam, the greater the increase in emittance. A plateau region of small growth is limited to below 1 mm mrad of initial normalised emittance. The size of the error bars are discussed in Subsection 5.2.3 .

kicking is applied, each particle in the grid is given the same  $p_x$  displacement but the weights are kept the same.

By simulating the original beam exactly at the fixed point position of the island, which is a relatively ideal situation, the steering error is eliminated so that the two sources of emittance growth (focusing error and steering error) can be separately investigated. It is found that the filamentation due to steering error dominates over that due to the focusing error, as the latter is only limited to a few percent growth. Therefore, it is critical that the positions of the islands are as close to  $x = 0$  m as possible to reduce this source of emittance growth. Moreover, since the kicker can only kick in one direction, the  $x$ -positions of the top and bottom islands must be simultaneously at 0 to reduce emittance growth over the entire kick process.

The effect of the initial emittance value on the growth of the emittance is investigated. Fig. 4.4 illustrates that, for very small beam sizes ( $< 0.1$  mm mrad), the emittance growth is governed by the focusing error, but at larger initial emittances ( $> 1$  mm mrad), the emittance growth increases less quickly with larger island surface. The plateau region is slightly larger for larger surfaces. Hence, the surface of the islands should be as large as possible while still satisfying other constraints.

From the results of the filamentation analysis, a configuration with a large island centred on  $x = 0$  m is optimal. The constraint on the optical parameters can be relaxed, as its effect is not dominant for the beam size of interest.



## 4.4 Parameter Scans

The horizontal and vertical chromaticities of the island need to be both negative below transition, and both positive above transition. However, it is observed that in most cases the horizontal and vertical chromaticities of the islands ( $DQ1_{is}$  and  $DQ2_{is}$ ) have opposite signs. Only rarely, when varying  $DQ1_{nom}$  and  $DQ2_{nom}$ , as well as the vertical tune, it is possible to have  $DQ_{is}$ 's of the same sign. This complicates the problem as these parameters also change the fixed point positions, the optical parameters, the momentum compaction, etc.

To summarise: we have the adjustable parameters:

- octupole(s) strength ( $k_3$ )
- matched horizontal chromaticity in the nominal (central) fixed point ( $DQ1_{nom}$ )
- matched vertical chromaticity in the nominal (central) fixed point ( $DQ2_{nom}$ )
- horizontal tune ( $Q_x$ )
- vertical tune ( $Q_y$ ).

The effects of these are investigated separately. The goal of these parameter scans is to find a configuration that has chromaticities of the same sign, and transition energy difference as large as possible. The island phase and surface are then checked afterwards.

### 4.4.1 Nominal Chromaticity

The chromaticities at the nominal fixed point are scanned at a fixed octupole strength and tune configuration. Note that the nominal chromaticities also need to be of the same sign, either negative below the transition or positive above the transition. It is observed in Fig. 4.5 that the larger the size of the nominal chromaticities,  $DQ_{nom}$ , the larger the size of the island chromaticities,  $DQ_{is}$ . Also shown in Fig. 4.5, the transition energy is mainly controlled by the horizontal chromaticity  $DQ1_{nom}$ ; and  $DQ2_{nom}$  has only a very small effect. In addition, increasing the sum of the nominal chromaticities decreases the surface of the island. It is already established that there is a tight constraint from the chromaticities and the transition energy. Therefore, from these observations, the region most promising to find both  $DQ_{is}$  of the same sign is at a small  $DQ1_{nom}$  value. However, in turn this gives a very small  $\Delta E_{tr}$ . A scan holding  $DQ1_{nom}$  constant and varying  $DQ2_{nom}$  is shown in Fig. 4.6. Since lower values of  $DQ2_{nom}$  give island chromaticities closer to 0, there is a greater chance of finding both positive and both negative chromaticities on the islands. Therefore, a value of 0.005 or -0.005 is chosen for  $DQ2_{nom}$ , depending on whether  $DQ1_{nom}$  is positive or negative. The scan of  $DQ1_{nom}$  then has to be combined with other parameter scans to decide a suitable value.  $DQ2_{is}$  is in the vertical plane, thus not coupled to the other parameters.

### 4.4.2 Octupole Strengths

By scanning the strength of individual octupoles, the dependence of the transition energy, fixed point positions, and island chromaticities fits a quadratic relation with less than 1% difference between the simulation and the quadratic fit for each data point. However, when simulating the contributions of two octupoles, there is no longer a quadratic relationship. Instead, it is found that there is a dependence on the sum of the octupole strengths. This agrees with what was discussed previously in Eq. (3.6).

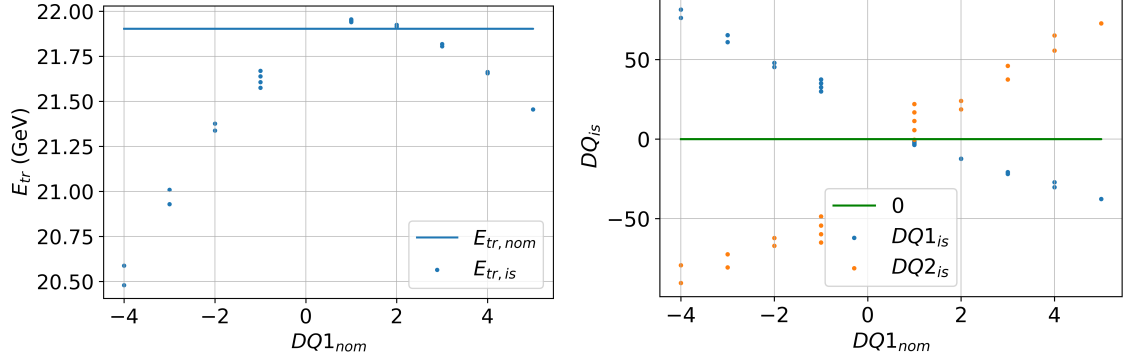


Figure 4.5: Scans of  $DQ1_{nom}$  and  $DQ2_{nom}$  of the LOE.12002+LOEN.52002 pair, for both islands at strength of  $-1.8 m^{-4}$ ,  $Q_x = 26.748$ . Left: Island transition energy as a function of  $DQ1_{nom}$ , Right: island chromaticities. The horizontal axis is  $DQ1_{nom}$  as both island chromaticities and transition energy are mainly dependent on the  $DQ1_{nom}$ , the vertical variation at each point is the variation along the  $DQ2_{nom}$  (scanned for the same range as  $DQ1_{nom}$ ).

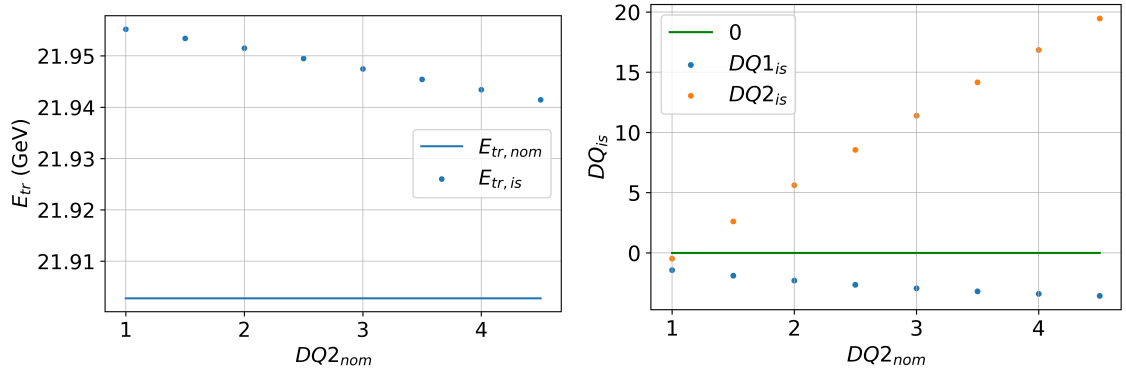


Figure 4.6: Variation of  $DQ2_{nom}$  for  $DQ1_{nom}$  fixed at 1, both islands  $k_3 = -1.8 m^{-4}$ ,  $Q_x = 26.748$ . Left: dependence of the island transition energy on  $DQ2_{nom}$ . Right: dependence of both  $DQ_{is}$ 's on  $DQ2_{nom}$ . The variations with  $DQ2_{nom}$  in this figure correspond to the vertical variation in Fig. 4.5 and therefore show that  $DQ1_{nom}$  takes the dominant control over the island chromaticities and transition energy. Note that as  $DQ1_{nom}$  is fixed to 1, negative  $DQ2_{nom}$  values are not scanned as the combination will be unusable.

The fixed point condition is controlled by the factor  $\Omega_2$ , which is a sum of the octupole strengths scaled by  $\beta_x$  at the location of the octupole. The values of  $\beta_x$  are very similar for the chosen octupoles, so the difference made by scaling is negligible. The sum of the values of  $k_3$  is enough to describe the dependence. However, the exact functional dependence on this sum is unclear and further testing would must be undertaken to unravel this. Importantly, it is found that for configurations with more than two octupoles, the ratio of the strengths of the octupoles can be used to control the phase of the islands, but within a range. Therefore, from the octupole combinations identified previously with a good phase, combinations of two octupoles are chosen to investigate further. As each additional octupole introduces one more degree of freedom, two octupoles give the flexibility of controlling the phase but do not introduce too many more parameters to complicate the problem. The pairs of octupoles chosen for further analysis are LOE.12002+ LOE.22002, LOE.12002+LOE.32002, LOE.12002+LOEN.52002, and LOE.32002+LOEN.52002. These are all pairs that were previously identified with  $|x| < 0.01$  m with both octupoles  $k_3 = 0.6\text{m}^{-4}$ ,  $Q_x = 26.747$ .

The study of octupole strength is combined with the nominal chromaticity to give the plots in Figs. 4.7, 4.8, and 4.9. Transition energy graphs show that it is possible to achieve more than 0.5 GeV difference in transition energy when  $E_{\text{tr, is}} < E_{\text{tr, nom}}$ . This means that when the beam has reached the nominal transition energy, it is already above transition on the island. This will require  $DQ_{1\text{is}}$  and  $DQ_{2\text{is}}$  to be both positive. However, this is not observed. In fact, the only possible solution to the chromaticity problem is at low values of  $k_3$ , where the  $DQ_{1\text{is}}$  and  $DQ_{2\text{is}}$  curves for the islands cross. This happens around where the island transition is above that of the nominal fixed point. There is a very small range of sum values of  $k_3$  where the  $DQ_{\text{is}}$ 's are both negative. For  $DQ_{1\text{nom}} = 3$ ,  $DQ_{2\text{nom}} = 0.005$ , there is a  $0.4\text{m}^{-4}$  window where this is satisfied.

This tight constraint on the chromaticities means that it is not possible to reach the 0.5 GeV energy difference target by changing the nominal chromaticities and the octupole strengths. However, increasing the nominal chromaticity does give a larger energy difference. At higher nominal chromaticities, the  $k_3$  sum value that gives both negative  $DQ_{\text{is}}$ 's also shifts to lower values, which means more disturbance to the system. Too much disturbance causes chaos, which is explained later in Section 4.5. The largest  $DQ_{1\text{nom}}$  in which there is no chaos at the  $DQ_{\text{is}}$  crossing point (where the  $DQ_{\text{is}}$ 's are both negative) is 3. Therefore, to maximise the energy difference while ensuring minimal chaos, the combination of nominal chromaticities should be fixed at  $DQ_{1\text{nom}} = 3$ ,  $DQ_{2\text{nom}} = 0.005$ .

It seems throughout this scan that it is only possible to achieve both negative chromaticities in the island (stable fixed point) and not both positive.

The pair of octupoles that fulfils the above requirements, while providing the highest energy difference and without chaos at  $DQ_{\text{is}}$  crossing are LOE.12002+LOEN.52002.

#### 4.4.3 Horizontal Tune $Q_x$

There is freedom to change the fractional part of the tunes as that does not significantly effect the cell optics and are controlled by a special quadrupole family. The integer part of the tune is controlled by the main quadrupoles and should be kept at the nominal value of 26 to avoid introducing too much change to the nominal fixed point.

There are two sets of tunes, the 0.25 resonance and the 0.75 resonance which both give the fourth-order resonance. The two sets are investigated separately. The scans in Figs. 4.10 and 4.11 show that the 0.75 resonance gives more promising configurations as there are regions where both  $DQ_{\text{is}}$ 's are below zero. When varying  $Q_x$  below the 0.75 resonance, it is found that the further away from resonance, the larger the amplitudes of  $DQ_{\text{is}}$ . The maximum of the island transition

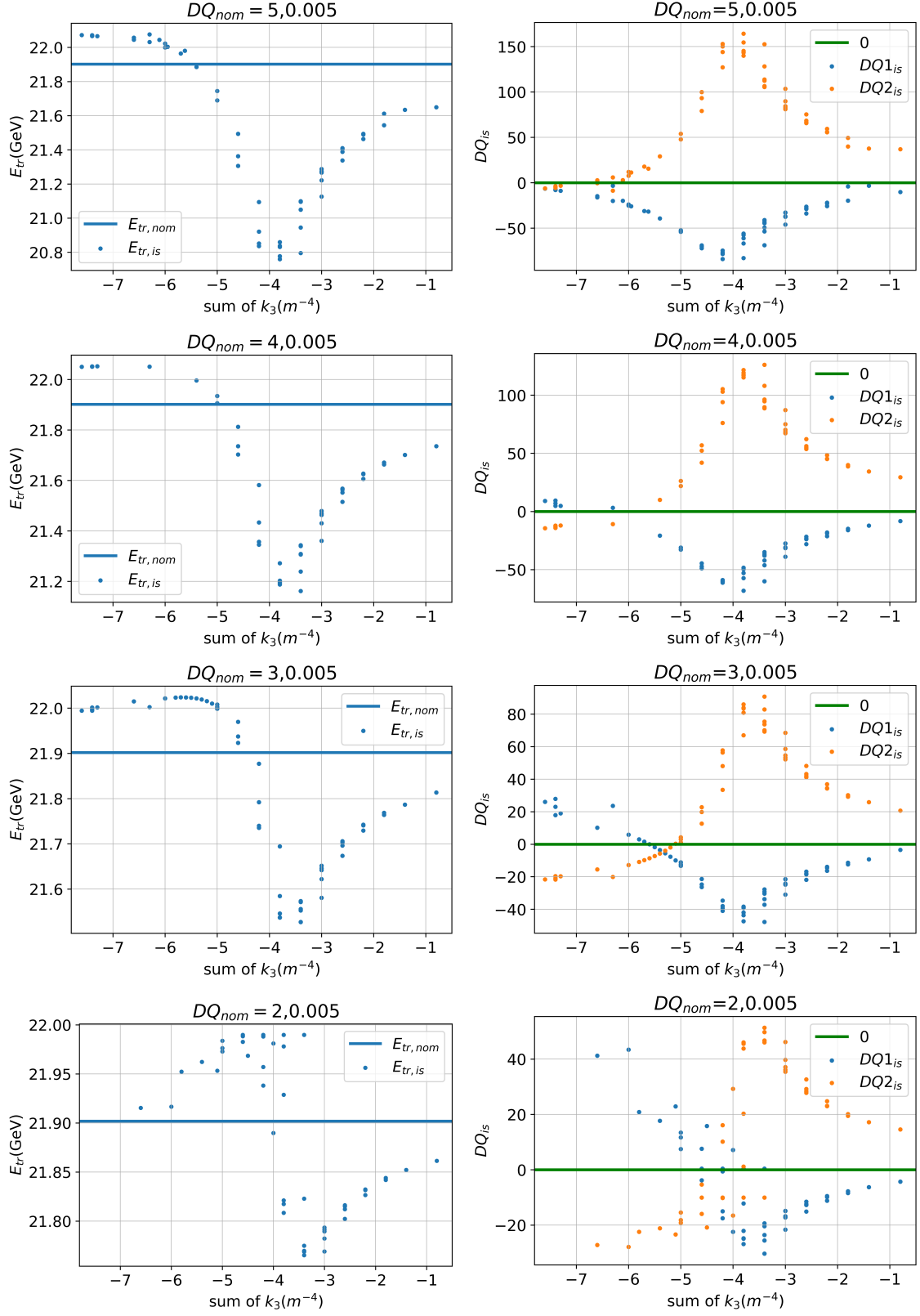


Figure 4.7:  $DQ_{nom} = DQ1_{nom}, DQ2_{nom}$ ;  $Q_x = 26.7495$ ,  $Q_y = 26.58$ . Scan for different  $DQ1_{nom}$  to see the effect on the constraints of transition energy and island chromaticities. The aim is to find a region where both  $DQ_{is}$  are the same sign and maximise  $\Delta E_{tr}$

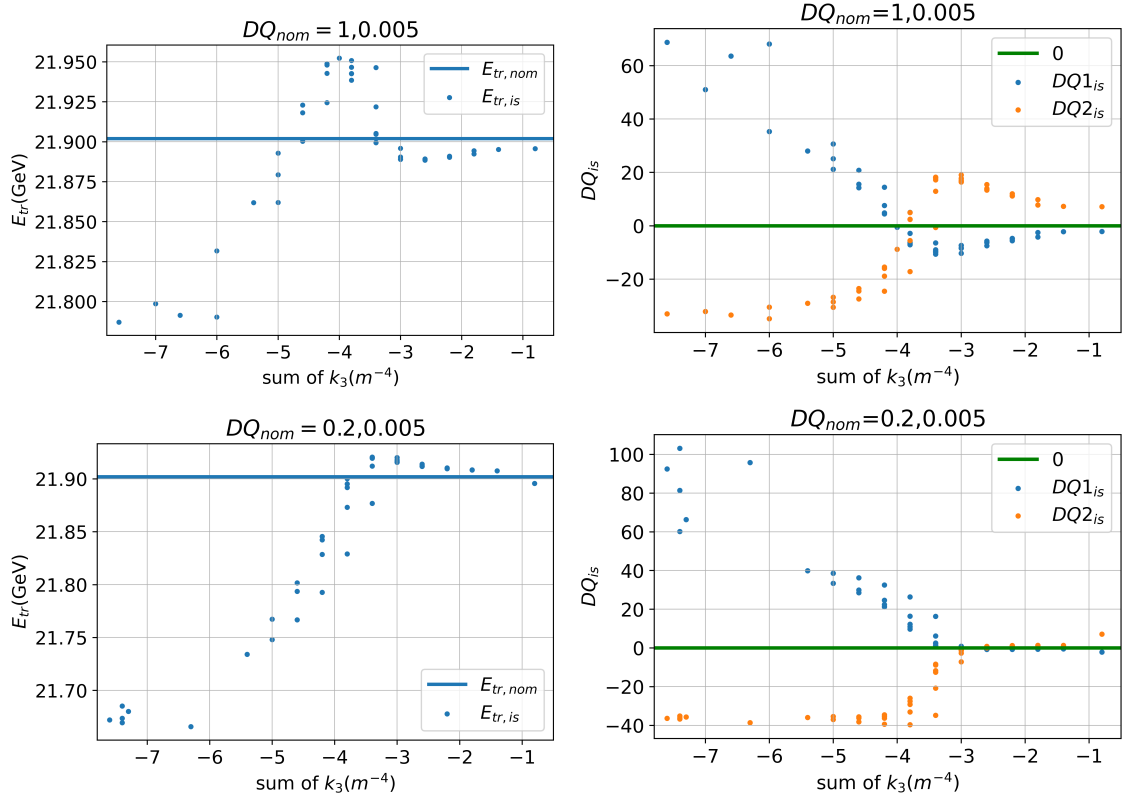


Figure 4.8:  $DQ_{nom} = DQ1_{nom}, DQ2_{nom}$ ;  $Q_x = 26.7495$ ,  $Q_y = 26.58$ . Continued scan for different  $DQ1_{nom}$ 's to see the effect on the constraints of transition energy and island chromaticities. The aim is to find a region where both  $DQ_{is}$  are of the same sign and maximise  $\Delta E_{tr}$

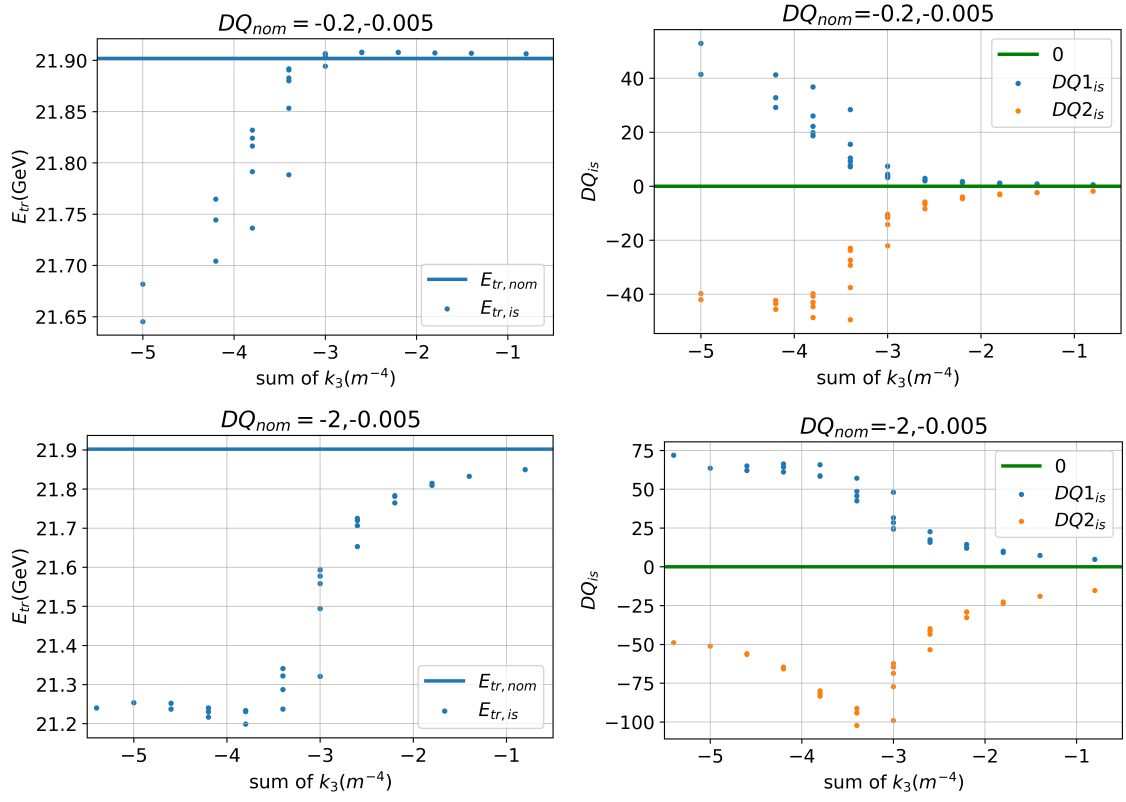


Figure 4.9: Continued scan for negative  $DQ1_{nom}$ 's to see the effect on the constraints of transition energy and island chromaticities. Given machine constraints, there is no region when both island chromaticities are the same sign within this range.

energy is also slightly higher the further away from resonance, and the crossing point of the  $DQ_{\text{is}}$ 's shifts towards less negative  $k_3$  values. However, as previously seen in Eq. (3.8), as the tune moves away from resonance,  $\Delta$  increases and hence the islands move further away from the centre. This causes more disturbance and hence chaotic behaviour is observed at lower  $k_3$  values.  $Q_x=26.747$  gives configurations where the optimum ratio of central surface and island surface, and also the largest  $\Delta E_{\text{tr}}$  before the system becomes chaotic, hence this value is chosen.

#### 4.4.4 Vertical Tune $Q_y$

There is also freedom to change the fractional part of the vertical tune which is also controlled by special families of quadrupoles, without significant alterations to the optics. As there is negligible coupling between the vertical plane and the other planes, this change should not have much effect on the islands in the horizontal plane and hence can be useful to adjust parameters in the vertical plane independently. Indeed varying the fractional part of  $Q_y$  does not change the island surface, fixed point position, transition energy or  $DQ1_{\text{is}}$  within requirements. The only significant impact is on  $DQ2_{\text{is}}$ , and this can be useful when  $DQ1_{\text{is}}$  is negative and  $DQ2_{\text{is}}$  has a small positive value, to bring the  $DQ2_{\text{is}}$  value to below zero. An example where this is achieved is shown in Fig. 4.12. However this can only be used in a very small number of cases as the adjustable range is very limited, and hence the value is kept at  $Q_y = 26.58$  which avoids low-order resonances in the vertical plane. The integer part, 26, is the nominal value for the SPS.

### 4.5 Chaos/ Beam Loss

When the octupole strength is too large, there is too much disturbance to the system such that the phase-space enters a chaotic regime, where the chaotic layer near the separatrix grows, hence more particles' motion become chaotic. In the chaotic layer, particle motion is unpredictable in a larger indistinct layer around the separatrix instead of following the orbits of constant hamiltonian. Other times the particle is lost after tens or hundreds of turns, where as the energy ramp in the SPS requires the order of  $10^5 - 10^6$  turns. The scenarios are demonstrated in Figs. 4.13, 4.14. The system becomes chaotic or the tracked particle is lost at different combinations of the above parameters, and there is not yet a clear pattern of combination of parameters that gives chaos. Further investigation would be needed to quantify this behaviour.

### 4.6 Summary of Search

The adjustable parameters are nominal horizontal chromaticity  $DQ1_{\text{nom}}$ , nominal vertical chromaticity  $DQ2_{\text{nom}}$ , LOE.12002 strength, LOEN.52002 octupole strength, horizontal tune  $Q_x$ , and vertical tune  $Q_y$ . The initial constraints on each are that the  $DQ1_{\text{nom}}$  and  $DQ2_{\text{nom}}$  are the same sign, and that the integer part of  $Q_x$  and  $Q_y$  are 26.

To determine optimum values for each of the parameters, they are scanned in the order of  $DQ_{\text{nom}}$ ,  $k_3$ , then  $Q_x$ .

The  $DQ_{\text{nom}}$  scans show that the island properties are mainly controlled by  $DQ1_{\text{nom}}$ . Scanning together with the sum of the octupole strengths, it is more likely to reach regions of both  $DQ1_{\text{is}}$  and  $DQ2_{\text{is}}$  to be negative at small  $DQ_{\text{nom}}$  values, but there is a greater transition energy difference for larger values of  $DQ1_{\text{nom}}$ . Hence, the  $DQ_{\text{nom}}$  values are chosen to be  $DQ1 = 3$ ,  $DQ2 = 0.005$ .

Then the  $k_3$  relationships are investigated by scanning the horizontal tune  $Q_x$ , 26.747 is chosen for the largest transition energy difference before chaos, and also a similar ratio of island and centre

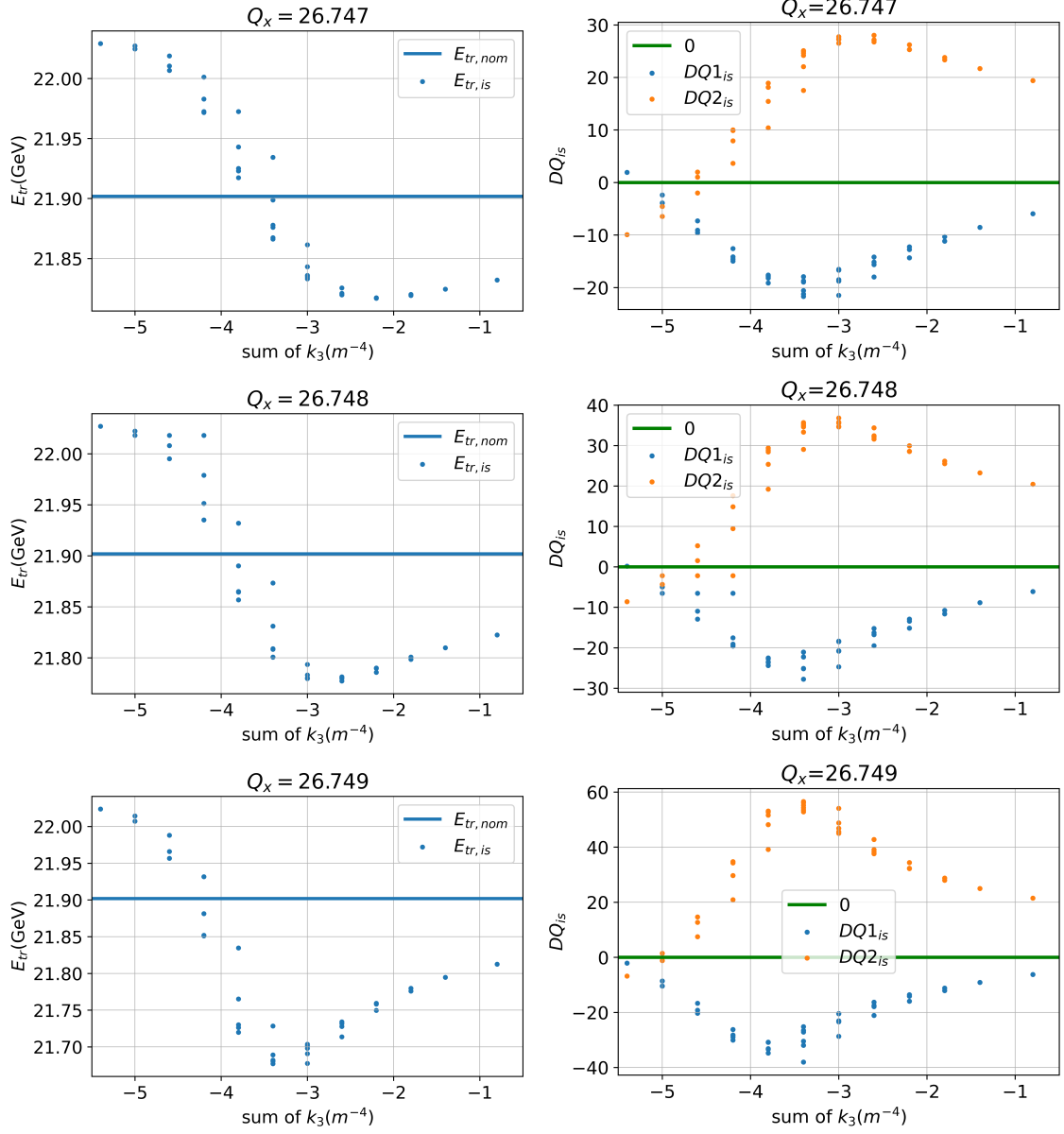


Figure 4.10:  $DQ_{1nom} = 3, DQ_{2nom} = 0.005, Q_y = 26.58$ , Scan of different  $Q_x$  near the 0.75 resonance to see the effect on the constraints of transition energy and island chromaticities. Aiming to find larger  $\Delta E_{tr}$  while  $DQ_{is}$ 's are still the same sign.



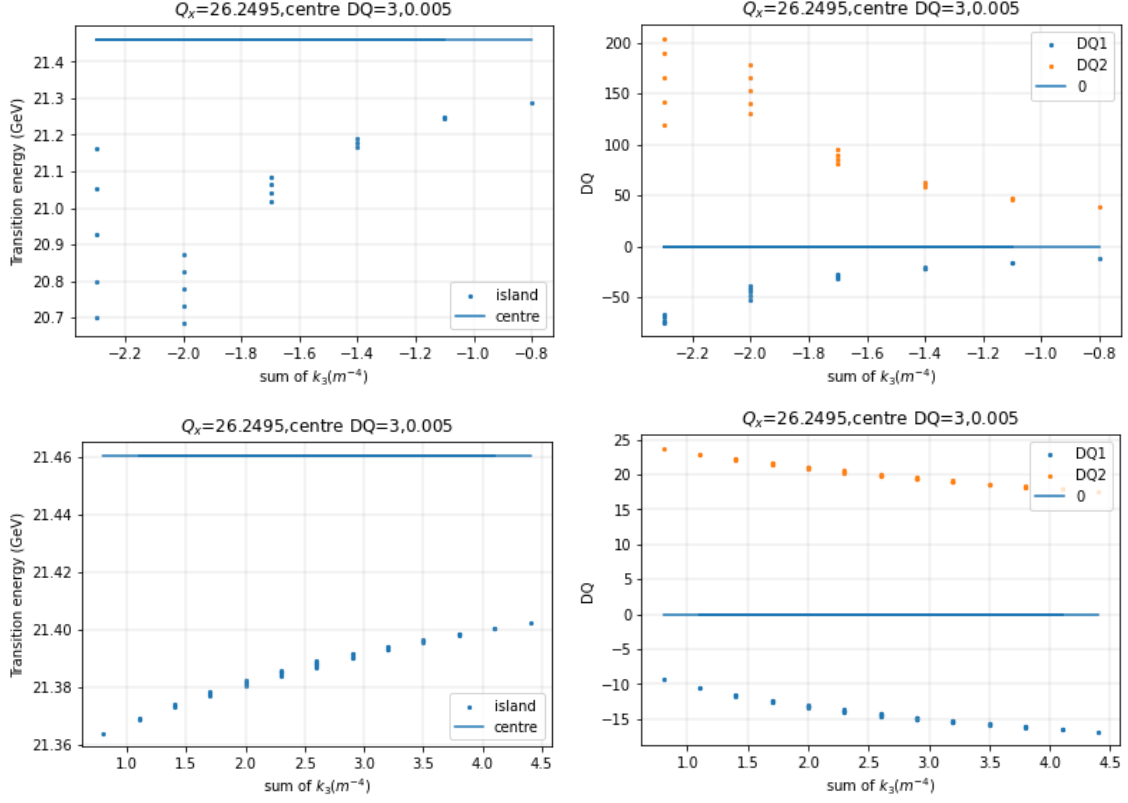


Figure 4.11:  $DQ1_{nom} = 3, DQ2 = 0.005, Q_x=26.2495, Q_y=26.58$ . Scan of positive and negative  $k_3$  values for one  $Q_x$  value near the 0.25 resonance. This shows that 0.25 series do not give more promising results than the 0.75 resonance. Top: negative octupole strengths. Bottom: positive octupole strengths.

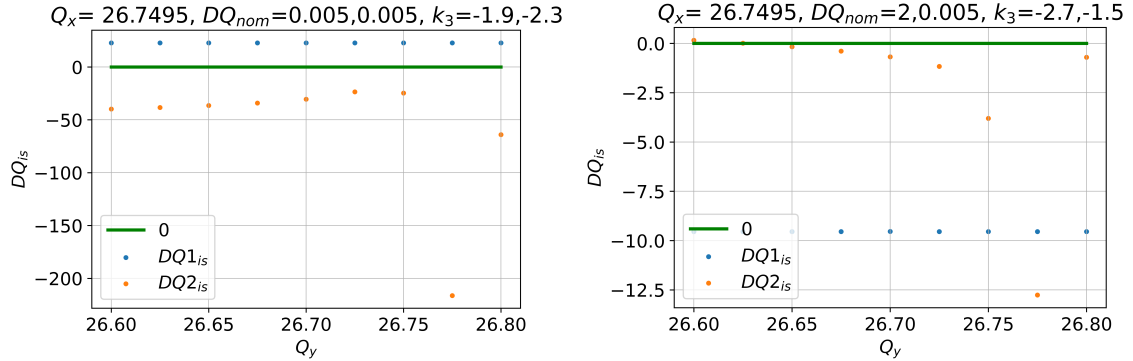


Figure 4.12: Effect of changing the vertical tune  $Q_y$  with all other parameters kept constant for two different configurations. It is possible to bring a small positive  $DQ2_{is}$  down to below 0 but not a small negative  $DQ2_{is}$  up to above 0.

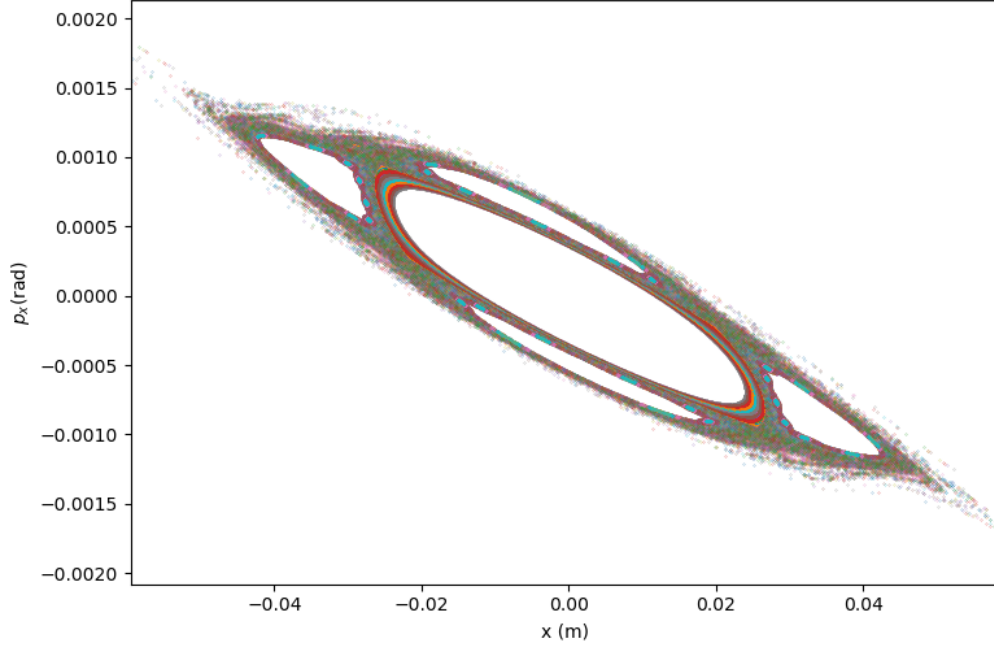


Figure 4.13: An example of the system becoming chaotic. The regions near the separatrix becomes more diffuse in phase space and particles no longer follow orbits of constant action. Different colours represent different tracked orbits.

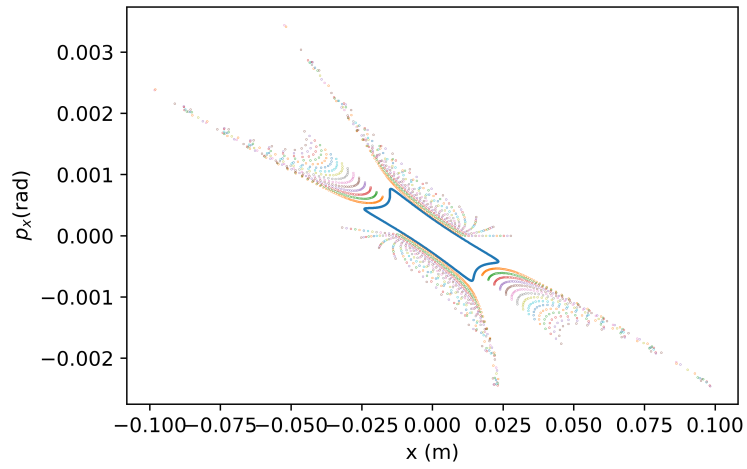


Figure 4.14: Example where there is too much disturbance and tracked particles are lost. There are not enough turns tracked before the loss and hence the orbits inside the islands are not completed.

region surface.

Finally, to achieve minimum emittance growth from a steering error, the phase is changed by changing the individual octupole strengths while keeping the sum constant, the minimum is when the bottom island is placed at  $x = 0$  m. This configuration will be used for above transition (henceforth denoted Config. 2), as the nominal chromaticities are positive.

Then it only remains to find another configuration (Config 1) with overlapping islands, and with nominal chromaticities below 0 for below transition. There are no constraints on the island chromaticities for this configuration as ideally the configuration switch will take place the same time the beam is kicked into an island, that is, directly into Config 2's island. The head-tail instabilities would not have developed before switching to the configuration with both island chromaticities below 0. Config 1's island transition energy is hence irrelevant as well. As all sets of nominal chromaticities can give overlapping islands with Config 2, the nominal chromaticities of Config 1 are chosen to be  $DQ1_{\text{nom}} = -0.2$ ,  $DQ2_{\text{nom}} = -0.005$  so that there is minimal difference between the two configurations, to minimise the disturbance caused by the switch of configurations.

It would be useful for future research to model the behaviour of the optics, the chromaticities, fixed point positions, and transition energy of islands based on the parameters investigated. This way, similar investigations will only need to input the target constraints, and the model will calculate the configurations.

# Chapter 5

## Results and Discussions

### 5.1 Final Identified Configurations

As it is not possible to reach the target of a transition energy difference of at least 0.5 GeV, two approaches are taken, one to maximise  $\Delta E_{\text{tr}}$  and the other to minimise the growth of the emittance. Hence, two sets of configurations are identified. For both sets, it is identified that the least overall emittance growth is when the bottom fixed point is placed exactly at 0. The method is then to kick into the bottom island first, switch the configuration once the beam is kicked into an island, and kick the beam back to the centre once transition is crossed and when the beam is in the top island. Kicking into the bottom island first ensures that there is minimal filamentation after the first kick, and reduces the overall emittance growth, as the emittance growth scales with the beam size. Only octupole strengths need to be changed when performing the chromaticity jump, and hence the other parameters are kept constant. The centre transition energy for both is 21.901 GeV.

#### 5.1.1 Maximising $\Delta E_{\text{tr}}$ Approach

As previously identified, to maximise  $\Delta E_{\text{tr}}$  without reaching chaos, and also satisfying the other constraints (previously stated in Chapter 4), the nominal chromaticities should be  $DQ1_{\text{nom}} = 3, DQ2_{\text{nom}} = 0.005$ . The octupole strengths' values in Table 5.1 are the ones that give both negative  $DQ_{\text{is}}$ 's and give the bottom island's fixed point as close to  $x = 0\text{m}$  as possible.

	Config. 1	Config. 2
$DQ1_{\text{nom}}, DQ2_{\text{nom}}$	-0.200, -0.005	3.000, 0.005
$DQ1_{\text{is}}, DQ2_{\text{is}}$	26.181, -33.091	-5.646, -2.628
$k_{3,1} \ k_{3,2}(m^{-4})^1$	-1.732, -2.479	-1.957, -2.918
$Q_x$	26.747	26.747
$Q_y$	26.580	26.580
Island $E_{\text{tr}}$ (GeV)	-	22.020
Island Surface (mm mrad)	$57 \pm 3$	$57 \pm 3$

Table 5.1: Parameters for the two configurations identified to maximise  $\Delta E_{\text{tr}}$ , the transition energy of Config. 1's islands is not relevant and hence is not presented. Note that the simulated values directly from MAD-X have negligible errors, and hence are not shown. Island surface uncertainties are discussed in Subsection 5.2.2.

With this configuration, a grid of particles is tracked as described in Section 4.3, and each is assigned a Gaussian weight to represent an initial Gaussian beam. To keep the filamentation

<sup>1</sup> $k_{3,1}$  and  $k_{3,2}$  denotes the strengths of the LOE.12002 and LOEN.52002 octupoles, respectively

growth to a minimum, the beam is first kicked into the bottom island, ends up on the top island, and then kicked back to the centre. A switch of configuration occurs when the beam is inside the islands. To allow the beam to fully filament at in each process, the beam is tracked for 8192 turns in the SPS lattice (with two more turns, 8194 turns when the beam ends up at the top island from the bottom one).

There are three stages of filamentation growth: 1) when the beam is kicked into the bottom island, 2) when the configuration switch occurs, and 3) when the beam is kicked back to the centre. The three-stage filamentation process is shown in Fig. 5.1. As expected, the first two stages do not incur significant emittance growths, with the first stage a percentage growth of 6.8% and the second stage a growth of only 1.7%. The growth of these two stages is designed to a minimum in the choice of the parameters. However, in the last stage, because the top island's fixed point is further away from  $x = 0$  m, the percentage increase in emittance is 682%. The overall growth in emittance from the transition crossing process is 749% reaching a final normalised emittance of  $8 \pm 1$  mm mrad, which is a very large growth and is not ideal.

### 5.1.2 Minimising Emittance Growth Approach

	Config. 1	Config. 2
$DQ1_{\text{nom}}, DQ2_{\text{nom}}$	-0.200, -0.005	1.000, 0.005
$DQ1_{\text{is}}, DQ2_{\text{is}}$	6.870, -16.789	-2.000, -1.690
$k_{3,1} \ k_{3,2}(m^{-4})$	-1.336, -1.586	-1.403, -1.687
$Q_x$	26.747	26.747
$Q_y$	26.580	26.580
$E_{\text{tr}}$ (GeV)	-	21.954
Island Surface (mm mrad)	$22 \pm 1$	$22 \pm 1$

Table 5.2: Parameters for the two configurations identified to minimise emittance, the transition energy of Config. 1's islands is not relevant and hence is not presented. Note that simulated values directly from MAD-X have negligible errors hence are not shown. Island surface uncertainties are discussed in Subsection 5.2.2.

This approach seeks to find a configuration with both islands as close to  $x = 0$  m as possible while satisfying the other constraints. This means that the search will be targeted at smaller islands and hence the region of low  $|k_3|$  values. In turn, this means the compromise of  $\Delta E_{\text{tr}}$ . As seen from the scans of  $DQ_{\text{nom}}$  in Figs. 4.7 and 4.8, when the values of  $DQ1_{\text{nom}}$  are low, the crossing point of the  $DQ_{\text{is}}$  occurs at lower  $|k_3|$  values.  $DQ1_{\text{nom}} = 1$  is hence the best choice since below that value the islands are not large enough to accommodate the beam. The other parameters are kept the same, and Config. 1 is again found by finding values of  $k_3$  giving  $DQ1_{\text{nom}} = -0.2, DQ2_{\text{nom}} = -0.005$  that give islands that overlap with our identified Config. 2.

The emittance growth of stage 1 is 16%, almost double the stage 1 growth for the other approach. As the islands in Config. 2 are small compared to the beam size, the beam experiences more non-linear effects associated with the edge of the island. The second stage a growth of 0.2 % which is a very little growth as expected, as the islands overlap almost perfectly. The third stage has a much larger emittance growth of 115%, resulting in a overall emittance growth of 150% which is smaller than the previous approach. The final emittance in this approach is  $2.50 \pm 0.01$  mm mrad.

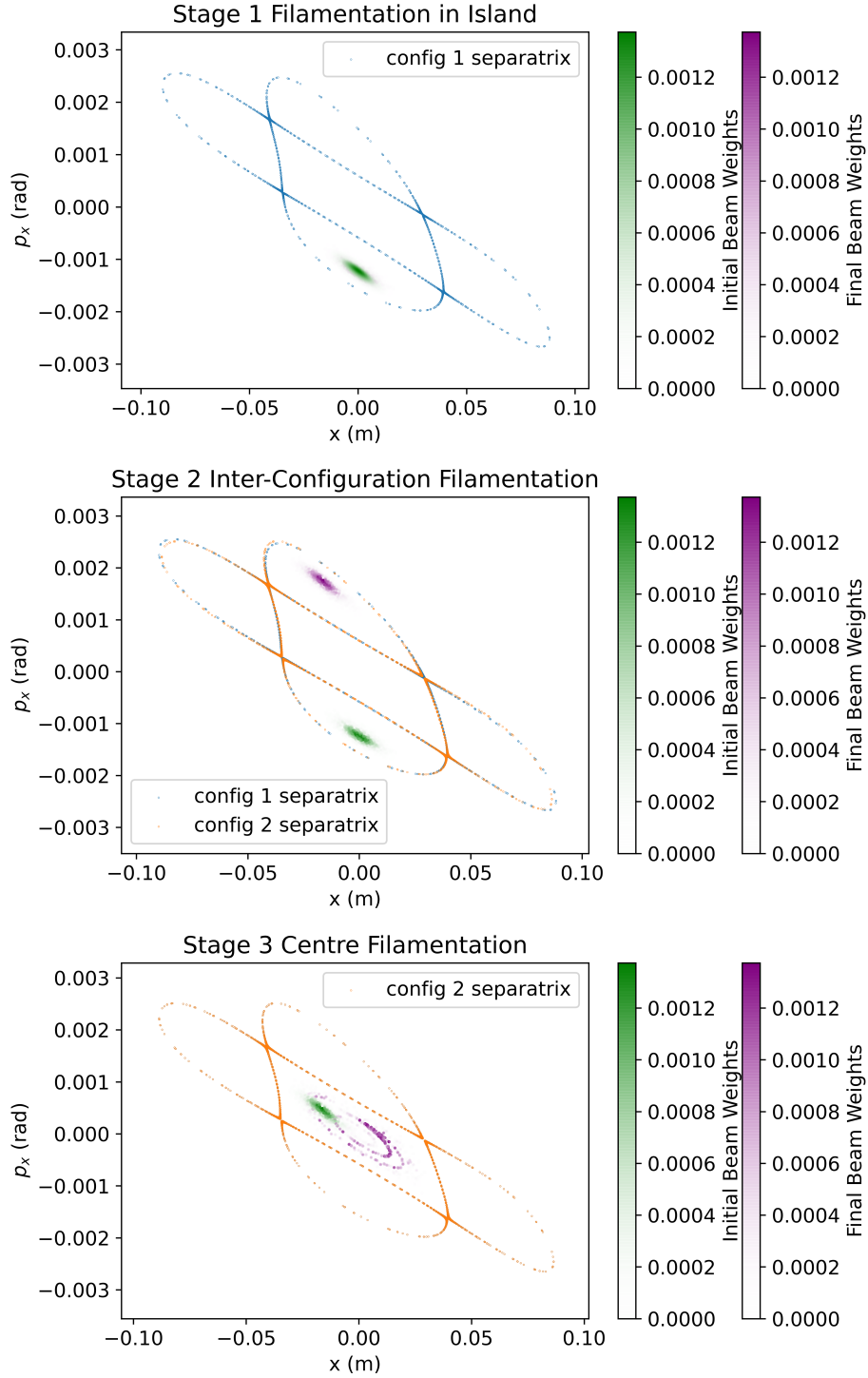


Figure 5.1: Three stages of emittance growth of the set of configuration that maximises  $\Delta E_{tr}$ . Top: filamentation after being kicked into island from centre. Middle: filamentation at switch of configuration. Bottom: filamentation when kicked back to centre from top island. The overall emittance growth is 749%.

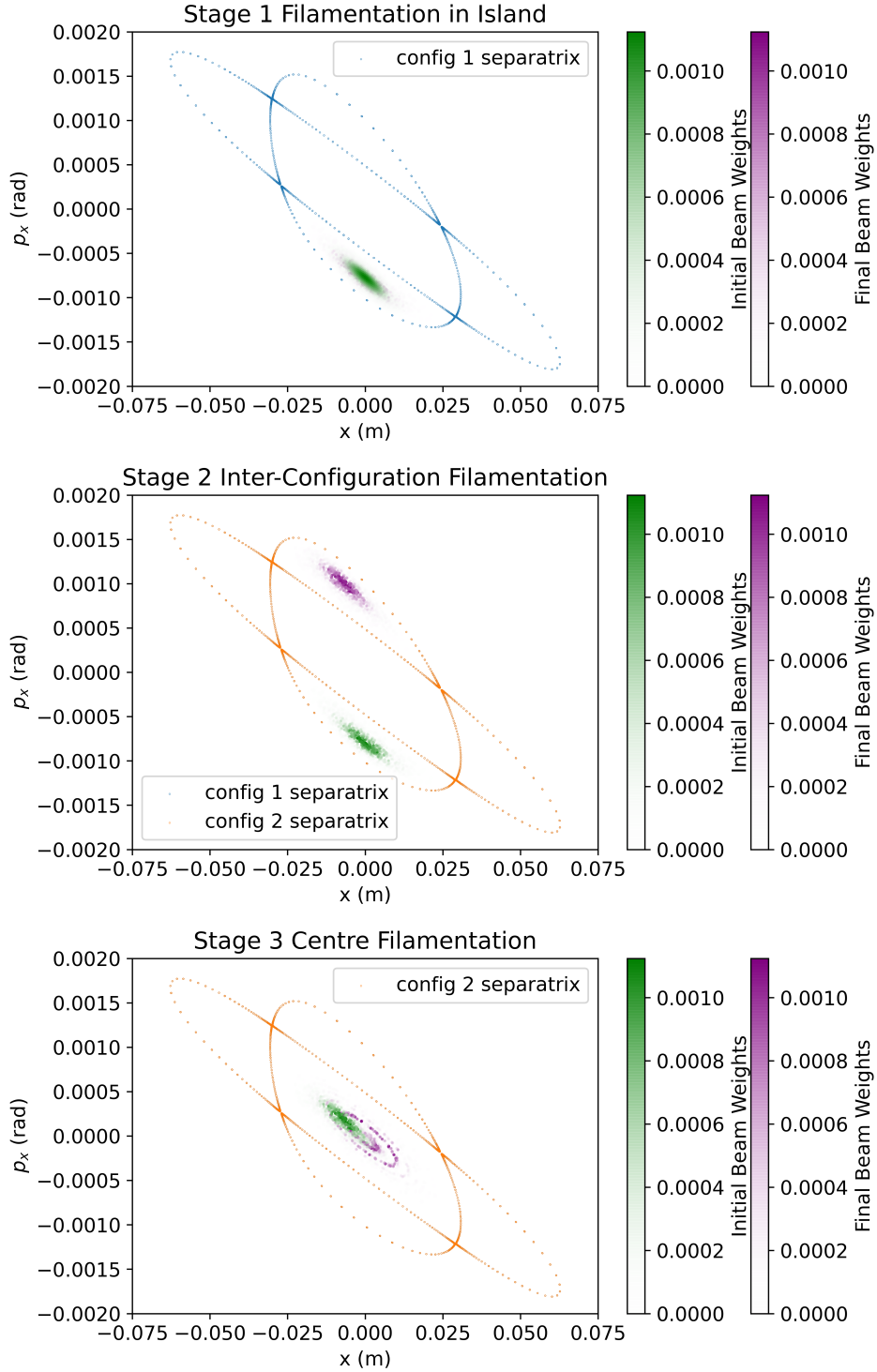


Figure 5.2: Three stages of emittance growth of the set configurations that minimises the filamentation. Top: filamentation after being kicked into island from centre. Middle: filamentation at switch of configuration. Bottom: filamentation when kicked back to centre from top island. The overall emittance growth is 150%

## 5.2 Uncertainty Analysis

### 5.2.1 MAD-X simulations

As the nature of this project is a simulation, the uncertainties from the simulation come from the models used in the programme. PTC is the most accurate simulation tool available, and hence the uncertainty of the results would be associated only with the numerical errors, which are on the order of  $10^{-15} - 10^{-16}$ . The difference of the simulation to the real lattice is in the magnetic errors from the SPS which is hard to estimate [32].

### 5.2.2 Island Surface Uncertainty

There are two sources of uncertainty for the separatrix method for surface estimation, which was previously established (in Subsection 4.2.1) as the most accurate method. The first is from how close the identified separatrix orbit is to the true separatrix, which depends on the density of the tracked grid of initial conditions. A grid of 360 initial conditions that spans a phase-space surface of 4.5 mm mrad is used for all surface calculations. To estimate an uncertainty, the four initial conditions in the grid that are nearest to the separatrix are identified, and their difference is calculated. The largest difference is taken as the uncertainty that estimates an error of at most 6%.

The second source of uncertainty on the island surface is the number of turns tracked. As the more turns MAD-X tracks, the more points there are on the phase-space plots to trace out the separatrix, hence the better the accuracy. A convergence test is done to test the number of turns necessary to give an accurate and converged surface. The results are summarised in Fig. 5.3, and one can conclude that 10000 turns is sufficient. After 10000 turns the variation is on the scale of  $10^{-4}$  mm mrad which is 0.009 % of the calculated surface. The uncertainty from this is negligible compared to the uncertainty from the identification of the separatrix orbit.

Due to the fact that there is no additional treatment of uncertainty levels, the precision of the calculated surface is kept to the level of the first non-zero digit of the error.

### 5.2.3 Emittance Uncertainty

The uncertainty in the calculation of the emittance comes from the density of the grid of points of initial conditions. The more dense the grid, the better the Gaussian distribution can be described by putting weights on each point. A convergence study is done on a beam of 1 mm mrad initial emittance, the standard beam size in the SPS. This is shown in Fig. 5.4. With more than 2000 data points in the grid with a surface of 89.22 mm mrad, the variation in the emittance is within 0.7%, hence this is taken as the uncertainty for this beam size. The same procedure is used for each initial beam emittance in Fig. 4.4 and the emittance values in this section, and the variation above 2000 data points is taken as the uncertainty. The precision of emittance calculations is also kept to the first non-zero digit of the uncertainty, as explained above.

### 5.2.4 Goodness of Fit

As the all data in this project is simulated, a chi-squared analysis of the goodness of fit is not possible. Instead, the root mean squared error is used as a measure of the absolute size of the error, and the percentage error at each point is calculated as a general goodness of fit.



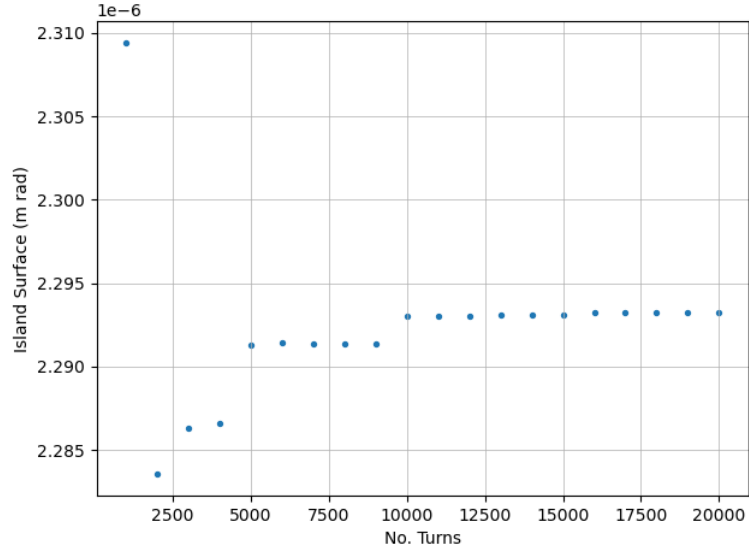


Figure 5.3: Convergence of the island surface calculated using the separatrix method with the number of turns tracked in the machine. Above 10000 turns the variation becomes negligible and so 10000 turns are used.

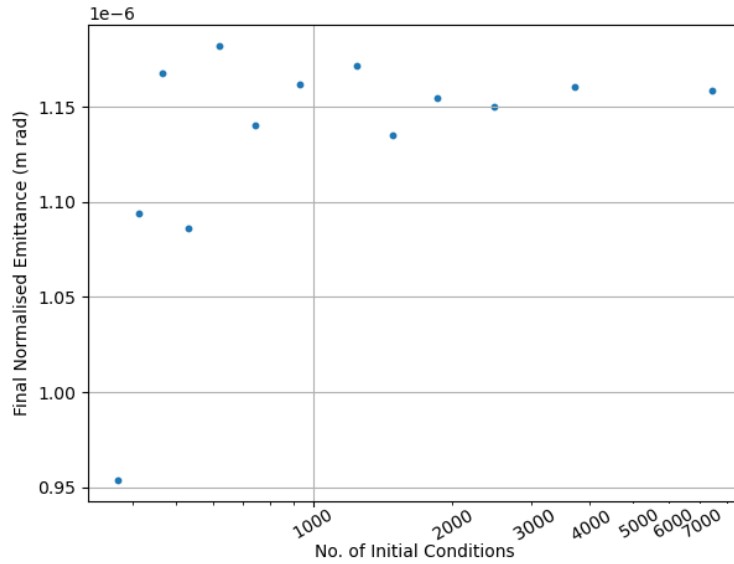


Figure 5.4: Convergence of the calculated final normalised emittance for a 1 mm mrad initial beam for the stage 1 filamentation for the minimising emittance growth approach. After 2000 points, the variation in the calculated value is within 0.7% and this is taken for the uncertainty.

### 5.3 Discussions on the Method

For such a complex system, it is necessary to make simplifying assumptions to uncover important effects. It is necessary to discuss the impact and validity of these assumptions.

First of all, the simulations are completed based on the perfect, error-free accelerator lattice, however, in the real SPS, magnetic errors are inevitable, hence it is possible that some constraints are no longer satisfied in the real machine with the configurations found in this project, for example the island chromaticity. Hence the parameters should be tested and adjusted accordingly if tested in the real machine.

Secondly, the time to kick the beam as well as the time to switch configurations are neglected, as the beam would have filamented based on the conditions at the time. For a precise overview of the filamentation, the simulation would need to be done turn by turn and the octupole and sextupole strengths to be changed based on the speed of changing the configuration and the speed of the kick. This is not a feature of MAD-X and hence the change of magnet strengths at each turn needs to be calculated before input to MAD-X. This will be a complicated and time-consuming process. The rise time for the MKQH kicker is of the order of a few  $\mu s$  or lower [33], and is of the order of a few  $s$  for the ramp time of the sextupole and octupoles [32]. In comparison, the SPS revolution time is  $2\pi R/c = 23.1 \mu s$ . This means that the kick time can be safely neglected. On the other hand, the time to switch configurations would be on the same time scale as the ramp time of the magnets, which is a few seconds [32]. This is not negligible considering the revolution period of the SPS of  $23.1 \mu s$ . However, the implication of this is simply that the beam would not have filamented fully, and hence the filamentation would be smaller than that of the simulation.

The energy ramp rate for SPS is  $3 \text{ MeV/turn}$  [32]. As the island transition energy is higher than that of the centre, it is necessary for the kick from the island back to the centre to be performed in between the two transition energies to avoid crossing either transition. This limits the time window when the kick back from island to centre can happen. This is a 40-turn window for the maximising  $\Delta E_{tr}$  approach and an 18-turn window for the minimising filamentation approach. However, this is not a problem for the kick process- how early the beam is kicked into the islands is not limited, and this would be chosen to allow enough time to switch configurations. The only effect would be that, as the beam is still close to transition after being kicked back, it could still experience some effects near transition.

Moreover, there is not enough flexibility in the lattice to place both islands at  $x = 0 \text{ m}$  which renders the emittance growth very large, and hence directly reduces the beam intensity. A solution to the problem would be to make the kicker bipolar (able to kick in both directions). This way only one island is required to be at  $x = 0 \text{ m}$  to ensure minimal emittance growth, as the beam would be kicked into and out of the same island, that is at  $x = 0 \text{ m}$  [34].

During the transition process, when Config. 1 is switched to Config. 2, an RF-phase jump must be performed to ensure phase stability as described in Section 2.3. Existing phase jump methods such as the compensated phase jump scheme [35] are designed to perform the phase jump for fast transition crossing with the gamma-jump schemes [35]. The compensated phase jump scheme is able to achieve the phase inversion in just one revolution period of the PS, which is safe to assume to be instantaneous and no phase instability will be incurred. However, this does require additional calculation of the exact point during the configuration switch at which the phase jump should be performed.

The coupling effect to the vertical plane is checked by plotting the phase-space diagrams for the plane, and an example is shown in Fig. 5.5. There are no islands or signs of non-linear disturbance to this plane, and hence it is indeed safe to neglect the transverse coupling. Regarding the lon-

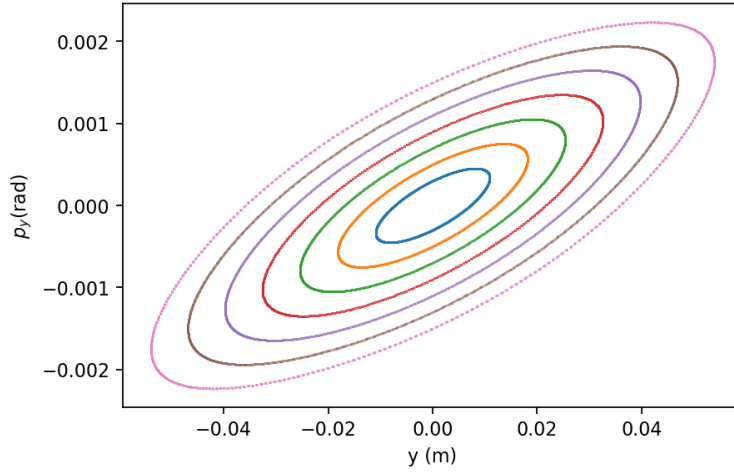


Figure 5.5: Phase-space of the y-plane for Config. 1 of the maximising  $\Delta E_{\text{tr}}$  approach, no islands are observed.

gitudinal plane, it would require very complex numerical simulations to quantify the disturbance to this plane including the bunch length oscillations as well as the transition energy spread due to space charges. They are not done in this project due to time limitations. However, it is essential to verify whether the proposed  $\Delta E_{\text{tr}}$  is large enough to avoid the effects near the transition, hence a future project could be based on analysis of the longitudinal beam dynamics of transition crossing by means of stable islands.

These discussions conclude that most of the assumptions made are justified. The only exception being the time dependence of the configuration switch, which would only mean an emittance growth less than that predicted in Subsections 5.1.1 and 5.1.2. As the method has not been experimentally tested, the size of magnetic errors is hard to quantify, and hence an experiment should also be designed to investigate this.

## Chapter 6

# Conclusions and Outlook

This project investigated the feasibility of a novel method to crossing transition energy simulated on the realistic SPS lattice. This method would solve problems such as changing the nominal tune with other transition-crossing methods; and if promising, should lead to experimental testing of the method. The project aimed to find a configuration of nonlinear magnets that would create stable islands in the transverse phase space. The islands would accommodate the entire beam and avoid beam losses and emittance blow-up while crossing the transition energy in circular synchrotron accelerators. The method has been successfully demonstrated in a proof-of-principle test on the PS lattice. It suggested that with a more flexible accelerator lattice, such as the SPS, a desired configuration can be found that would ensure sufficient transition energy difference without beam losses and large emittance growths. Indeed it is seen again that the additional fixed points generated by the non-linear magnets demonstrate a different transition energy to that at the centre (nominal fixed point), as well as different optics to that at the centre. Within the scope of this project, no configuration that satisfies all constraints was found. A number of limitations were identified, principally the limit from island chromaticities, leading to compromises on emittance growth or transition energy differences. Instead, two configurations were studied in details optimising each of the compromised values. The first to optimise  $\Delta E_{tr}$  uses larger islands and results in  $\Delta E_{tr} = 0.118$  GeV but the fixed points are further from  $x = 0$  m and hence gives an overall 749% emittance growth. The second approach minimises the growth of the emittance using smaller islands to give an overall growth of 150% , but gives a smaller transition energy difference of  $\Delta E_{tr} = 0.052$  GeV.

It is clear that both configurations have limitations that must be considered. As both island transition energies are above that of the centre and the energy difference is very small, the energy would still be near transition when the beam is kicked back to the centre and could still experience the disruptions typical when near transition energy. The emittance growth is also exceeding the tolerances, which would lead to an impact on the beam intensity and hence lower the quality of the physics experiments. The possibility of upgrading the MKQH kicker magnet to kick bidirectionally was discussed. With this made possible, the problem of emittance growth would be solved and then the focus can be shifted to maximising  $\Delta E_{tr}$ .

Since this method of crossing transition is still novel, many exciting future work could be completed to extend these studies further. As mentioned, a more rigorous analysis, including a full multivariate analysis involving all previously identified parameters, is required for effective identification of ideal machine configuration. A model of the transition energy and island chromaticities, as well as the chaotic layer's dependence on all these parameters, would be greatly beneficial. Moving forward, tests should be performed to see if  $\Delta E_{tr}$  of the identified configurations are large enough for the kick process to successfully avoid transition. An experiment could also be designed

to quantify the size of magnetic errors as well as the disturbance to the proposed configurations. Moreover, all feasible configurations identified have required negative island chromaticities. Further investigation is required to understand this and identify if positive island chromaticities are also possible. This could potentially solve the problem of not having enough difference in transition energy, as this means that  $E_{\text{tr, is}} < E_{\text{tr, nom}}$  and as seen in the parameter scans this allows for larger transition energy differences.

## Acknowledgements

I would like to thank my supervisor Massimo Giovannozzi for his guidance throughout this journey, for always checking up on me, and directing me in the right direction should I be caught up on immature ideas and irrelevant investigations. Also, we thank Hannis Bartosik, who gave many helpful insights on the SPS that are very hard to find in the literature.

I am also grateful for the help from the rest of the BE-ABP-NDC section for the useful discussions, insights, and always being happy to help. In particular, Dora Veres and Carlo Emilio Montanari, who helped me set up an efficient workflow for running simulations on HT Condor as well as gave many insights on the theoretical side of non-linear dynamics.

I also thank Tatiana Pieloni for setting up this project and always being there for advice and chats. Also, I thank Imperial College, EPFL, and especially my exchange coordinator Gavin Davies for this exchange opportunity.

# Bibliography

- [1] CERN, “Our mission - cern,” <https://home.cern/about/who-we-are/our-mission>, 2023, [Accessed on 21st June 2023].
- [2] G. Golluccio and J. Gournay, “Circular colliders,” in *Particle Accelerator Physics: Basic Principles and Linear Beam Dynamics*, H. Wiedemann, Ed. Springer, 2015, pp. 487–518.
- [3] S. Lee, *Accelerator physics (fourth edition)*. World Scientific, 2019.
- [4] R. Cappi and M. Giovannozzi, “Novel method for multiturn extraction: Trapping charged particles in islands of phase space,” *Phys. Rev. Lett.*, vol. 88, p. 104801, Feb 2002. [Online]. Available: <https://link.aps.org/doi/10.1103/PhysRevLett.88.104801>
- [5] M. Giovannozzi, L. Huang, A. Huschauer, and A. Franchi, “A novel non-adiabatic approach to transition crossing in a circular hadron accelerator,” *Eur. Phys. J. Plus*, vol. 136, no. 11, p. 1189, 2021. [Online]. Available: <https://cds.cern.ch/record/2779959>
- [6] M. Martini, “An introduction to transverse beam dynamics in accelerators,” CERN, Geneva, Tech. Rep., 1996. [Online]. Available: <http://cds.cern.ch/record/2853814>
- [7] E. Wilson and B. Holzer, *Beam Dynamics*, 05 2020, pp. 15–50.
- [8] R. Bossart, J. P. Delahaye, and A. Hofmann, “Measuring the Chromaticity from Head-Tail Oscillations,” CERN, Geneva, Tech. Rep., 1988. [Online]. Available: <https://cds.cern.ch/record/2854319>
- [9] D. Möhl, “Sources of emittance growth,” 2006. [Online]. Available: <https://cds.cern.ch/record/1005037>
- [10] T. Risselada, “Gamma transition jump schemes,” 1994. [Online]. Available: <https://cds.cern.ch/record/261069>
- [11] F. Tecker, “Longitudinal Beam Dynamics in Circular Accelerators,” Tech. Rep., 2020, figure 6: Energy gain as a function of particle phase; oscillations are stable around the synchronous-phase particle P1 below transition and around the synchronous-phase particle P2 above transition. 17 pages, contribution to the CAS - CERN Accelerator School: Introduction to Accelerator Physics. arXiv admin note: substantial text overlap with arXiv:2004.11908, arXiv:1601.04901. [Online]. Available: <https://cds.cern.ch/record/2746987>
- [12] D. Mohl and M. Elias, *Transition Crossing*, ser. CERN Yellow Reports: Monographs. Geneva: CERN, 2011, pp. 59–68. [Online]. Available: <https://cds.cern.ch/record/1359959>
- [13] D. Trbojevic, D. Finley, R. Gerig, and S. D. Holmes, “Design method for high energy accelerator without transition energy,” *Conf. Proc. C*, vol. 900612, pp. 1536–1538, 1990.

- [14] L. Teng, “Infinite transition energy synchrotron lattice using pi straight sections,” *Part. Accel.*, vol. 4, pp. 81–85, 1972.
- [15] Y. Senichev, “The Lattice with Imaginary  $\gamma$ -Transition for the CERN Proton Synchrotron PS2,” 2008. [Online]. Available: <https://cds.cern.ch/record/1133374>
- [16] A. Bogacz, “Design of Imaginary Transition Gamma Booster Synchrotron for the Jefferson Lab EIC (JLEIC),” in *8th International Particle Accelerator Conference*, 5 2017.
- [17] P. Lefèvre, D. Möhl, G. Plass, and P. Lefèvre, “The CERN Low Energy Antiproton Ring (LEAR) project,” 1980. [Online]. Available: <https://cds.cern.ch/record/879246>
- [18] R. Cappi, S. S. Gilardoni, M. Giovannozzi, M. Martini, E. Métral, J. Morel, P. Scaramuzzi, R. Steerenberg, and A. S. Müller, “Multi-turn extraction based on trapping in stable islands,” 2005. [Online]. Available: <https://cds.cern.ch/record/925934>
- [19] R. Cappi and M. Giovannozzi, “Multiturn extraction and injection by means of adiabatic capture in stable islands of phase space,” *Physical Review Special Topics - Accelerators and Beams*, vol. 7, no. 2, p. 024001, 02 2004. [Online]. Available: <https://cir.nii.ac.jp/crid/1361981471410772736>
- [20] M. Giovannozzi and J. Morel, “Principle and Analysis of Multiturn Injection Using Stable Islands of Transverse Phase Space,” *Phys. Rev. Spec. Top. Accel. Beams*, vol. 10, p. 034001, 2007. [Online]. Available: <https://cds.cern.ch/record/1035231>
- [21] S. Gilardoni, M. Giovannozzi, M. Martini, E. Métral, P. Scaramuzzi, R. Steerenberg, and A.-S. Müller, “Experimental evidence of adiabatic splitting of charged particle beams using stable islands of transverse phase space,” *Phys. Rev. ST Accel. Beams*, vol. 9, p. 104001, Oct 2006. [Online]. Available: <https://link.aps.org/doi/10.1103/PhysRevSTAB.9.104001>
- [22] E. Lopienska, *The CERN accelerator complex, layout in 2022*. CERN, Feb 2022. [Online]. Available: <https://home.cern/science/accelerators/accelerator-complex>
- [23] CERN, “CERN accelerator complex,” <https://home.cern/science/accelerators/accelerator-complex>, accessed on 6th June 2023.
- [24] J. B. Adams, “The SPS: a European project,” 1974. [Online]. Available: <https://cds.cern.ch/record/862882>
- [25] L. Deniau, H. Grote, G. G. Roy, and F. Schmidt, “The MAD-X Program,” 2022. [Online]. Available: <https://cern.ch/madx/releases/last-rel/madxuguide.pdf>
- [26] F. Schmidt, E. Forest, and E. McIntosh, “Introduction to the polymorphic tracking code: Fibre bundles, polymorphic Taylor types and "Exact tracking",” CERN, Geneva, Tech. Rep., 2002. [Online]. Available: <http://cds.cern.ch/record/573082>
- [27] A. Bazzani, G. Servizi, E. Todesco, and G. Turchetti, *A normal form approach to the theory of nonlinear betatronic motion*, ser. CERN Yellow Reports: Monographs. Geneva: CERN, 1994. [Online]. Available: <https://cds.cern.ch/record/262179>
- [28] M. Giovannozzi, D. Quattraro, and G. Turchetti, “Generating unstable resonances for extraction schemes based on transverse splitting,” *Phys. Rev. ST Accel. Beams*, vol. 12, p. 024003, Feb 2009. [Online]. Available: <https://link.aps.org/doi/10.1103/PhysRevSTAB.12.024003>



- [29] R. Bartolini, A. Bazzani, M. Giovannozzi, W. Scandale, and E. Todesco, “Tune evaluation in simulations and experiments,” *Part. Accel.*, vol. 52, no. 3-4, pp. 147–177, 1996. [Online]. Available: <https://cds.cern.ch/record/292773>
- [30] E. Asseo, J. Bengtsson, and M. Chanel, “Absolute and high precision measurements of particle beam parameters at cern antiproton storage ring lear using spectral analysis with correction algorithms,” in *Fourth European Signal Processing Conference*, J. Lacoume and others (eds.), Eds., Amsterdam, 1988, pp. 1317–1320.
- [31] W. Press, S. Teukolsky, W. Vetterling, and B. Flannery, *Numerical Recipes: The Art of Scientific Computing*, 3rd ed. Cambridge, UK: Cambridge Univ. Press, 2007.
- [32] H. Bartosik, personal communication.
- [33] F. Caspers, E. Gaxiola, T. Kroyer, M. Timmins, J. Uythoven, and S. Kurennoy, “A retrofit technique for kicker beam-coupling impedance reduction,” 08 2004.
- [34] P. Collier *et al.*, “The SPS as injector for LHC: Conceptual design,” 3 1997.
- [35] H. Damerau, “Compensated Phase Jump at Transition Crossing in the CERN PS,” CERN, Tech. Rep., 2019, poster presented at LLRF Workshop 2019 (LLRF2019, arXiv:1909.06754). [Online]. Available: <https://cds.cern.ch/record/2699470>